AN ABSTRACT OF THE THESIS OF

James J. Osborne for the degree of Master of Science in Physics presented on October 22, 2004.

Title: Zinc Tin Oxide Thin Films by Pulsed Laser Deposition for use in Transparent Thin-Film Transistors

Abstract approved:

Redacted for Privacy

Dr. Janet Tate

Zinc tin oxide (ZTO) films deposited by pulsed laser deposition (PLD) are investigated as a channel layers for transparent thin-film transistors (TTFTs). Films are deposited on glass for characterization, and transistor channel layers are deposited onto aluminum oxide-titanium oxide/tin doped indium oxide/glass substrates (ATO/ITO/glass) to produce TTFTs.

UV-visible spectroscopy on films gives average T/(1-R) values around 80% at 500 nm and optical bandgaps between 3.03 and 3.7 eV. EPMA and RBS analyses show that the films consistently contain about 15% less zinc than the targets from which they are deposited. Van der Pauw measurements yield a minimum resistivity of 2.35 Ω-cm, and a maximum Hall mobility of 10.4 cm^2-V^{-1}-s^{-1}.

Annealing the TTFTs in air at 600 °C for 30 minutes improves performance. XRD analysis shows this anneal changes the amorphous ZTO to a mixture of amorphous ZTO and crystalline ZnO. The highest achieved mobilities for TTFTs produced are μ_{avg} = 6.63 cm^2-V^{-1}-s^{-1} and μ_{inc} = 8.35 cm^2-V^{-1}-s^{-1} with drain current on-to-off ratios in the 10^5 range.

© Copyright by James J. Osborne
October 22, 2004
All Rights Reserved

Zinc Tin Oxide Thin Films by Pulsed Laser Deposition for use in Transparent Thin-Film Transistors

by
James J. Osborne

A THESIS

submitted to

Oregon State University

in partial fulfillment of
the requirements for the
degree of

Master of Science

Presented October 22, 2004
Commencement June 2005

Master of Science thesis of James J. Osborne

presented on October 22, 2004.

APPROVED:

Redacted for Privacy

Major Professor, representing Physics

Redacted for Privacy

Chair of the Department of Physics

Redacted for Privacy

Dean of the Graduate School

I understand that my thesis will become part of the permanent collection of Oregon State University libraries. My signature below authorizes release of my thesis to any reader upon request.

Redacted for Privacy

James J. Osborne, Author

ACKNOWLEDGEMENTS

I would like to acknowledge all the support received from my thesis advisors, Dr. Janet Tate and Dr. John Wager and the entire research group I worked with. I especially thank Paul Newhouse for all the help and assistance using the pulsed laser deposition lab and taking the X-ray diffraction measurements.

I thank Dr. John Wager and his research group in Engineering for all the help with the production and analysis of transistor structures as well as a giving a general direction to the research I was conducting. I acknowledge the help from David Hong, Matt Spiegelberg, and Rick Presley for annealing and testing these TTFT channel layers. Special thanks to Matt Spiegelberg for all the extra help with the last-minute experiments and the careful analysis of the TFT measurements.

Thank you Robert Kykyneshi for the atomic force microscopy analysis and for transporting films and targets to and from Eugene.

Thanks to Cheol-Hee Park for making the PLD targets and giving me extra help with the XRD analysis and related discussions.

PLD substrate masks were fabricated by Ted Hinke, along with many other bits and pieces that were used in the PLD system. I would also like to think Ted Hinke and Joe Magner for all the help with the sputtering system overhaul project, which was my first introduction to vacuum systems.

Another thanks goes to Joe Magner for help with fixing the Hall measurement system.

Thanks to the people at the OSU EPMA lab and to John Donovan at the University of Oregon EPMA lab (CAMCOR) for help with the characterization of these thin films and targets.

I appreciate all the helpful discussions with Matt Price about writing this thesis, analyzing data (especially the Hall measurements), keeping the labs I worked in running, and other, much broader, topics.

Lastly, I thank my wife, Pauline, for her continual patience with me during this work.

Funding for this work was provided by the Army Research Office under MURI E-18-667-G3.

TABLE OF CONTENTS

Page

1 INTRODUCTION 1

2 LITERATURE REVIEW 4

3 FILM PRODUCTION AND DEVICE MANUFACTURING 7

3.1 Experimental Procedure 7

3.2 Results and Discussion 10

3.3 Summary 11

4 CHARACTERIZATION TECHNIQUES 12

4.1 Introduction 12

4.2 Electrical Transport Measurements 12

4.3 Optical Characterization 15

4.4 Compositional Analysis 16

4.5 X-Ray Diffraction 18

4.6 Atomic Force Microscopy 18

4.7 Transistor Analysis 19

5 FILM CHARACTERIZATION RESULTS 20

5.1 Introduction 20

5.2 Electrical Transport Measurement Results 21

5.3 Optical Characterization Results 24

5.4 Compositional Analysis Results 29

TABLE OF CONTENTS (Continued)

Page

5.5 X-Ray Diffraction Analysis Results ... 36

5.6 Atomic Force Microscopy ... 39

5.7 Summary ... 41

6 TRANSPARENT THIN-FILM TRANSISTORS ... 42

6.1 Introduction ... 42

6.2 Device Manufacture and Testing ... 45

6.3 Results and Discussion ... 47

6.4 Summary ... 53

7 CONCLUSIONS AND FUTURE WORK ... 55

7.1 Conclusions ... 55

7.2 Future Work ... 57

BIBLIOGRAPHY ... 59

APPENDICIES ... 62

PLD Deposited Films ... 63

Optical Characterization Results ... 64

EPMA Results for Targets ... 65

TTFT Characteristics ... 66

LIST OF FIGURES

Figure | Page

1.1 A thin-film transistor test structure. 2

3.1 PLD system vacuum diagram (top) and laser path to chamber (bottom). 7

3.2 PLD substrate masks. 9

4.1 Structure for van der Pauw measurements. 13

5.1 O_2 Pressure during deposition for three different targets of $Zn_{(2-x)}Sn_xO_{(4+y)}$ labeled 2, 2.2, and 1.8. 21

5.2 Enhancement-mode TFT showing conductive channel induced by a positive gate voltage. 23

5.3 Photoresistance of Zn_2SnO_4. 24

5.4 UV - visible (T/1-R) for various deposited films. 25

5.5 Absorption coefficient for a representative ZTO film. 26

5.6 Bandgap analysis. 27

5.7 Absorption coefficient for ZTO_023 (Appendix A) showing the region of the onset of absorption. 28

5.8 Carrier concentration versus optical bandgap energy for several ZTO films. 29

5.9 Zinc-to-tin ratios for all films measured. 30

5.10 SEM images of the 2:1 target. 31

5.11 SEM images of the 2.2:1 target. 32

5.12 SEM images of the 1.8:1 target. 32

LIST OF FIGURES (Continued)

Figure | Page

5.13 Zinc-to-tin ratios for films of three targets deposited at varying laser pulse energy densities. 34

5.14 Zinc-to-tin ratio versus oxygen deposition pressure for films ablated from three different targets. 35

5.15 Depth profile for film ZTO_011 analyzed by RBS. 35

5.16 XRD analysis of film ZTO_044 before and after annealing. . . . 37

5.17 AFM surface roughness maps. 40

6.1 TFT test structure. 43

6.2 Theoretical I_{ds}-V_{ds} curves for a typical enhancement-mode transistor. 44

6.3 I_{ds}-V_{ds} characteristics for transistor ZTO_038 (Appendix A). . . . 46

6.4 Transfer curve for transistor ZTO_042 (Appendix A). 47

6.5 I_{ds}-V_{ds} characteristics for transistor ZTO_045 from the first analysis (top) compared to the second analysis performed three days later (bottom). 49

6.6: A ZTO TTFT channel layer directly after 100 °C anneal, and after another week of storage. 50

6.7 I_{ds}-V_{ds} characteristics for a sputtered ZTO TTFT after processing (top), after one month in ambient conditions (middle), and after a 100 °C anneal (bottom). 51

6.8 Transmittance (direct) for three transistor channel layers on ITO/ATO/glass substrates. 53

LIST OF TABLES

Table Page

2.1 Properties of a few TTFT materials. 5

5.1 RBS results for the zinc-to-tin ratios compared with the
EPMA results. 36

LIST OF APPENDIX TABLES

Table — Page

A: PLD deposited films. 63

B: Transmittance, absorption coefficient, and results from the direct and indirect bandgap analyses for several ZTO films. 64

C: Summary of EPMA results for three ZTO targets. 65

D: μ_{avg}, μ_{inc}, source-drain current drive at 40 V gate voltage, and $I_{on:off}$ for the TTFT channel layers tested. 66

LIST OF ABBREVIATIONS

AFM	Atomic Force Microscopy.
AMLCD	Active matrix liquid crystal display
ATO	Aluminum oxide / titanium oxide layered film that serves as a gate insulator in TTFTs.
CTO	Cadmium tin oxide (Cd_2SnO_4), otherwise known as cadmium stannate.
EPMA	Electron Probe Microanalysis
HMS	Hall measurement system.
ITO	Tin doped indium oxide ($In_{2-x}Sn_xO_{3+y}$). Used as the gate layer in TTFTs.
PLD	Pulse Laser Deposition.
Ra	Average roughness in AFM analyses.
RBS	Rutherford Backscattering.
Rms	Root mean squared roughness in AFM analyses.
TCO	Transparent Conducting Oxide.
TFT	Thin Film Transistor.
TMP	Turbo Molecular Pump
TTFT	Transparent Thin Film Transistor.
UV	Ultra-violet. Electromagnetic radiation with wavelength range of 390 nm – 10 nm.
XRD	X-ray Diffraction.
ZTO	Zinc tin oxide (Zn_2SnO_4 – spinel $ZnSnO_3$ – orthorhombic), otherwise known as zinc stannate.

ZINC TIN OXIDE THIN-FILMS BY PULSED LASER DEPOSITON FOR USE IN TRANSPARENT THIN-FILM TRANSISTORS

Chapter 1
INTRODUCTION

Transparent conducting oxides (TCOs) are of interest for use in transparent electronics such as touch-screens, photovoltaic devices, and window defrosters. TCOs are wide-bandgap (E_{gap} > 3 eV) materials with conductivities (σ) up to 10^4 Ω^{-1}-cm^{-1}. Thin film TCOs are generally made by various deposition techniques such as chemical vapor deposition, magnetron sputtering, electron-beam sputtering, ion-beam sputtering, thermal evaporation, or pulsed laser deposition. The goal of vacuum deposition is to take a bulk material and deposit it onto a substrate slowly enough to grow thin films that are tens to hundreds of nanometers thick.

One application for transparent conductors is the transparent thin-film transistor (TTFT). TTFTs have been built using wide bandgap semiconductors such as ZnO, SnO_2 $InGaO_3(ZnO)_5$ and hydrogenated silicon channel layers (Hoffman 2004; Presley *et al.* 2004; Nomura *et al.* 2003).

One type of TFT consists of a substrate, gate conductor, gate insulator, channel layer, and source and drain contacts as shown in Figure 1.1.

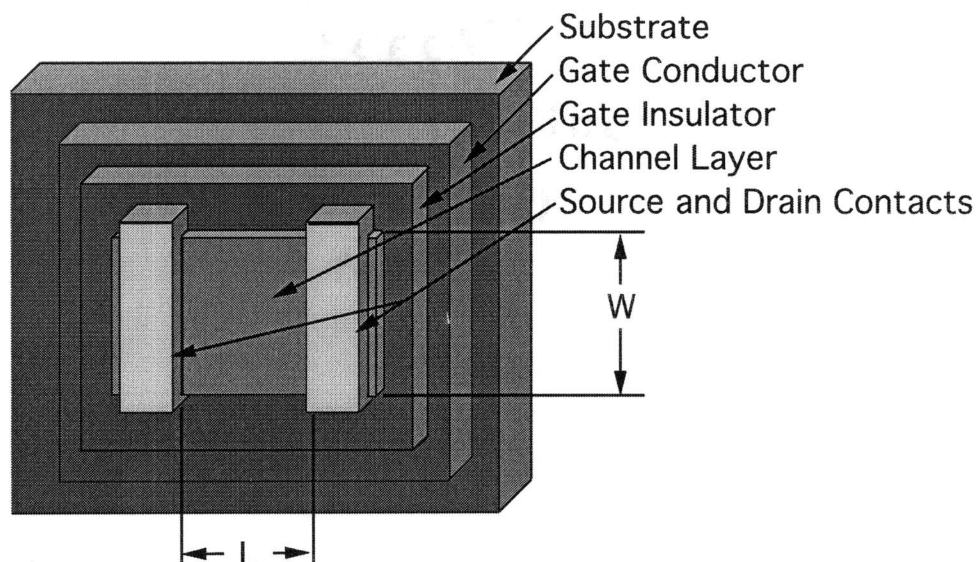

Figure 1.1: A thin-film transistor test structure.

For enhancement-mode devices, the channel layer must be electrically insulating in the absence of a gate bias. As a gate bias of appropriate polarity is applied, carriers are drawn to the semiconductor (channel layer) – insulator interface, creating a conducting channel. More discussion about field-effect devices can be found in Pierret (Pierret 1996).

The purpose of this thesis is to report on the investigation of zinc tin oxide (ZTO) for application as a channel layer in TTFTs. ZTO is reportedly electrically conductive and optically transparent (Perkins *et al.* 2002a; Wu *et al.* 1996), though in an amorphous state, ZTO can be insulating (Wu *et al.* 1996). For a channel layer in an enhancement-mode TTFT, the chosen material must be made insulating, but have a high mobility for carriers that are injected into the channel layer. For this reason, ZTO is of interest as a channel layer for enhancement-mode TTFTs. The literature for sputter deposited ZTO is fairly extensive, but for PLD films there are few reports.

For this project, a particular interest is to examine the effect on the performance of the transistors as the zinc-to-tin ratio in the targets is varied. A low temperature manufacturing process is ideal, so amorphous ZTO is deposited at

room temperature, but the best transistors are made from films that are post-deposition annealed at 600 °C. In order for a material to be a good candidate for a channel layer in a TTFT, it must have a wide energy bandgap (E_{gap} > 3.1 eV) so that it is transparent, a high resistivity (ρ ~ MΩ-cm), and a high carrier mobility for injected carriers. Several films are made under different deposition conditions and tested for electrical transport properties. After sufficient electrical transport data are gathered for the films, the conditions that produce the most promising films for TTFT channel layers are duplicated to make films of the correct structure for TTFTs.

To produce films, a pulsed laser deposition (PLD) system is used. Films are characterized for electrical transport, optical, and compositional properties. For electrical transport measurements, van der Pauw measurements are made with a Lakeshore Hall Measurement System (HMS). Resistivity and Hall coefficient are measured, and carrier concentration and Hall mobility are calculated from these measurements. UV-visible scans are made for optical characterization using a grating spectrometer. Compositional analysis of the films is carried out by electron probe micro-analysis (EPMA) and Rutherford backscattering (RBS).

The organization of this thesis is as follows. A literature review is given in Chapter 2. Details of film production and device manufacturing are given in Chapter 3. Film and device characterization techniques are outlined in Chapter 4. The film characterization results are given in Chapter 5 and the TTFT characterization results are given in Chapter 6. Chapter 7 gives final conclusions and discussion of this thesis, along with suggestions for future work.

Chapter 2
LITERATURE REVIEW

The most conductive TCO reported to date is tin-doped indium oxide (ITO) with a conductivity (σ) of 10^4 Ω^{-1}-cm^{-1} (Gordon 2000). Other TCOs include Cd_2SnO_4 (CTO) (McGraw *et al.* 1995; Nozik, Haacke 1976; Nozik 1974), tin oxide with dopants such as fluorine (Gordon 2000; Lytle, Junge 1951), antimony (Dates, Davis 1967; Mochel 1947), and chlorine (McMaster 1947), zinc oxide with dopants such as indium (Hu, Gordon 1993; Major *et al.* 1984; Qiu *et al.* 1987), gallium (Choi *et al.* 1990; Hu, Gordon 1992a), aluminum (Hu, Gordon 1992b; Minami *et al.* 1984; Minami *et al.* 1985), fluorine (Hu, Gordon 1990), and boron (Vijayakumar *et al.* 1988).

Two basic crystalline forms of ZTO are the cubic spinel phase with the stoichiometry Zn_2SnO_4, and the orthorhombic phase, which has the stoichiometry $ZnSnO_3$ (Young *et al.* 2002). The orthorhombic phase is unstable at high temperatures (400 °C), and decomposes into other phases (Perkins *et al.* 2002b). In this report, the Zn_2SnO_4 stoichiometry is examined, and referred to as "on stoichiometry."

ZTO is a wide bandgap semiconductor, with a fundamental bandgap of 3.35 eV for crystalline Zn_2SnO_4 (Young 2000). The highest reported conductivity for ZTO is 340 Ω^{-1}-cm^{-1} and the highest reported Hall mobility is 32 cm^2-V^{-1}-s^{-1} (Kluth *et al.* 2003). In that report, films of ZTO are RF magnetron sputtered in pure argon onto glass substrates which are heated to approximately 400 °C. It has also been shown that ZTO is very insulating if it is in the amorphous phase (Wu *et al.* 1996). For enhancement-mode transistor operation, the resistivity should be high in the absence of a gate bias, and a high mobility is required for carriers in the channel layer as a gate bias is applied. Because ZTO can be insulating and has a

moderate mobility when made conducting, it is a good candidate for an enhancement-mode device. More details regarding the structural characterization of ZTO can be found in Young, Williamson and Coutts's paper (Young *et al.* 2002).

There has also been interest in ZTO as a TCO due to its low price and availability whereas indium reserves are limited (Brown 2004). ZTO is also non-toxic unlike other TCOs such as cadmium stannate (Coutts *et al.* 2000).

The first thin-film transistor (TFT) was created by P.K. Weimer in 1962 (Weimer 1962). The TFT structure is entirely deposited onto a substrate rather than being built into a bulk material by doping specific regions. This allows for reduced cost of materials, since the insulating substrate can be inexpensive glass as opposed to high-purity silicon. A primary application for TFTs are active-matrix liquid crystal displays (AMLCDs). Amorphous silicon TTFTs are used in AMLCDs. A drawback to amorphous silicon as TTFTs is that they must be light-shielded. TTFTs that function while light is passing through them can significantly reduce the costs of manufacturing AMLCDs.

TFTs have been built using a variety of transparent semiconductors such as ZnO, SnO_2, and $InGaO_3(ZnO)_5$ (Hoffman 2004; Presley 2004; Nomura *et al.* 2003).

Results from studies of a few representative TTFT materials are summarized in Table 2.1.

Material	Mobility (cm^2-V^{-1}-s^{-1})	Current on:off ratio	Reference
Zn_2SnO_4	(FE) 20-50	10^6	Chiang 2003
ZnO	(avg, inc) 12, 25	$7x10^8$	Hoffman 2004
$InGaO_3(ZnO)_5$	(FE) 80	10^6	Nomura *et al.* 2003
SnO_2	(FE) 2.0	10^5	Presley *et al.* 2004

Table 2.1: Properties of a few TTFT materials. FE stands for field-effect mobility, avg and inc stand for average and incremental mobility, respectively. Mobility calculations are discussed in Chapter 6.

ZnO has been successful as a channel layer for a TTFT (Hoffman 2004; Hoffman *et al.* 2003; Masuda *et al.* 2003; Norris *et al.* 2003). The highest mobility reported for a ZnO channel layer in a TTFT is 25 cm^2-V^{-1}-s^{-1} (Hoffman 2004). $InGaO_3(ZnO)_5$ TTFTs have been demonstrated and are currently one of the highest performance TTFTs with peak mobilities around 80 cm^2-V^{-1}-s^{-1} (Nomura *et al.* 2003).

For ZTO, the best drain current on-to-off ratio to date is in the 10^8 range, and peak field-effect mobilities around 50 cm^2-V^{-1}-s^{-1}, although peak field-effect mobilities of 100 cm^2-V^{-1}-s^{-1} have been reported for depletion-mode operation (Chiang 2003), but not reproduced.

Chapter 3
FILM PRODUCTION AND DEVICE MANUFACTURING

3.1 Experimental Procedure

Films are produced by pulsed laser deposition (PLD) at Oregon State University's PLD laboratory. Schematics of the PLD system are shown below in Figure 3.1.

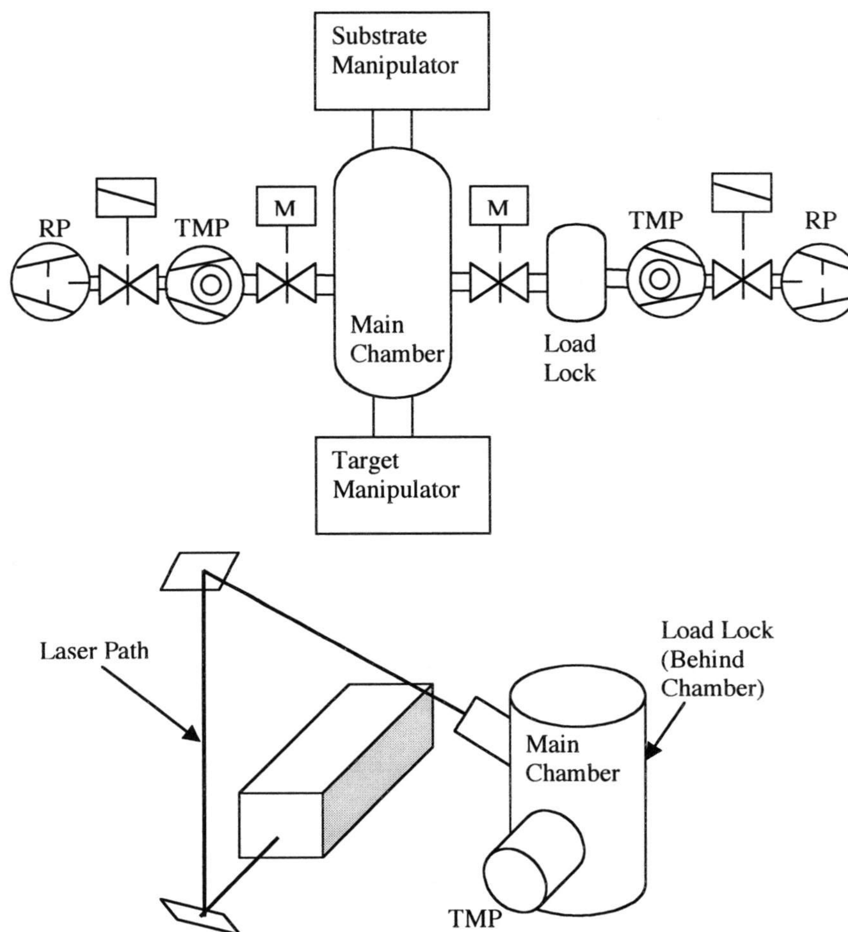

Figure 3.1: PLD system vacuum diagram (top) and laser path to chamber (bottom).

The PLD system employs a 248 nm KrF excimer laser and a UHV chamber built by Thermionics, Inc. based on a design by Dr. Hiroshi Yanagi. It became operational in September, 2003. The chamber is pumped by a turbo-molecular pump (TMP) (Boc Edwards STP-1003C) backed by a rotary vane pump. Base pressures in the 10^{-9} Torr range are achieved. Access to the chamber is gained via a load lock (see Figure 3.1). Laser pulses of wavelength $\lambda = 248$ nm and pulse width, $\tau = 20$ ns are generated by a Lambda Physik COMPex 201 UV KrF excimer pulsed laser and focused onto the top surface of a 1-inch nominal diameter ceramic target via an optical tower and lens apparatus. The target is rotated at approximately 90 rpm during depositions for uniform ablation. The 1-inch square substrate is held 2.25 inches above the target, and rotated at approximately 50 rpm during the deposition for more uniform film growth, though the films still vary in thickness with distance from the center of rotation. The thicknesses of the films are measured by profilometry in several locations. The variation in thickness from the middle to the edge of the film is between 16% and 67%. One of two different masks is placed over the substrate for the deposition in order to create structures for either transistor channel layers or electrical transport measurements. These masks are shown in Figure 3.2.

The targets used are manufactured by Choel-Hee Park (Keszler group, OSU Chemistry) from mixtures of ZnO (Cerac, 99.99%) and SnO_2 (Cerac, 99.99%) powder. The ratios, $ZnO:SnO_2$, are set to 1.8:1, 2:1, and 2.2:1 by mole ratio. The powders are mixed together by hand for approximately 10 minutes. Next the powder mixture is ground using a mechanical mortar and pestle for approximately 20 minutes. The powder is heated at 1100 °C for 5 hours, after which XRD analysis is performed. The product is then pressed into a 1 inch diameter by 3/16 inch thick pellet at 2 tons and put on an alumina plate.

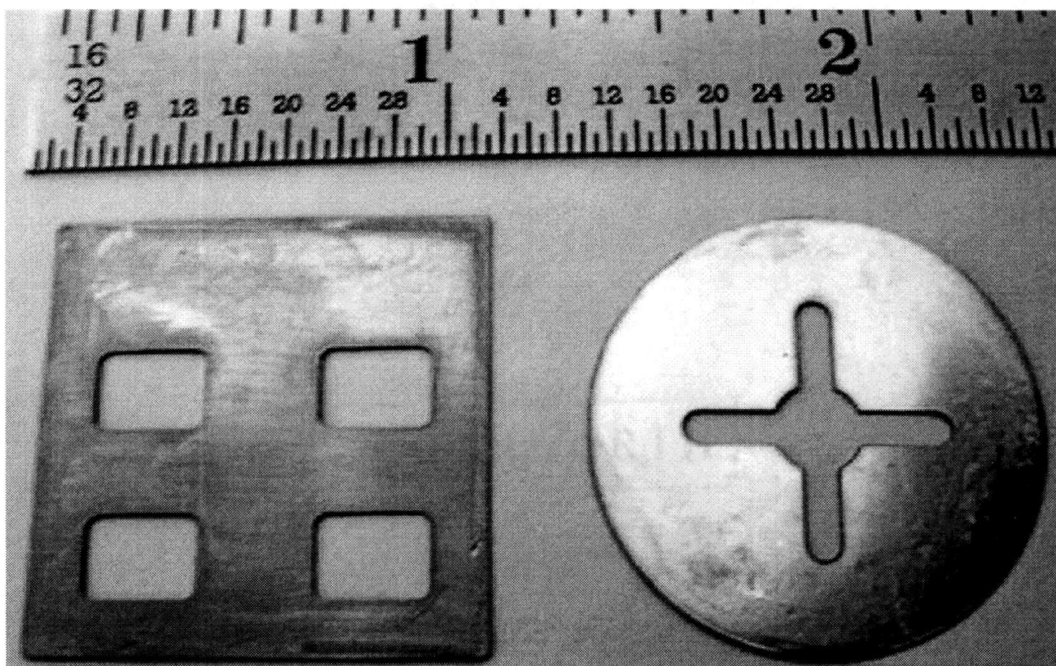

Figure 3.2: PLD substrate masks. On the left is the mask for transistor channel layers, and on the right is the cross structure for van der Pauw transport measurements.

Another alumina plate is put on top of the pellet, and the entire assembly is annealed at 1350 °C for 3 hours in air. This technique results in the synthesis of Zn_2SnO_4 by the following reaction.

$$2ZnO + SnO_2 \rightarrow Zn_2SnO_4 \quad (1)$$

In the case of the off-stoichiometry targets, the reaction is

$$(2+x)ZnO + SnO_2 \rightarrow Zn_{2+x}SnO_{4+x} \quad (2)$$

with x being 0, 0.2, or –0.2 for targets of Zn:Sn ratios of 2.0:1. 2.2:1, or 1.8:1, respectively. The target densities are 97%, 98.7%, and 94% for the 2.0:1, 2.2:1, and 1.8:1 targets.

Film depositions are usually carried out in an oxygen atmosphere, varying the pressure from 6 x 10^{-2} Torr to "vacuum". For the vacuum depositions, no oxygen is admitted into the system, but during the deposition, the chamber pressure

increases to around 5 x 10^{-7} Torr due to the ablation of the target during deposition. A deposition time of 10 minutes with laser pulses at 10 Hz is found to produce films around 200 nm in thickness as established by profilometry. This frequency and time is used for the majority of the films. Films are deposited on glass for characterization, or (ATO/ITO/glass) substrates for the measurement of its behavior as a transistor channel layer. These coated substrates are provided by Planar Systems. A 200 nm thick layer of ITO is sputtered on the glass substrate, followed by a 220 nm atomic layer deposited superlattice of Al_2O_3 and TiO_2. The ITO is the conducting layer for the gate, and the ATO layer is the gate insulator.

3.2 Results and Discussion

Film production and characterization occur together, so the process of making films is guided by the results from various characterization techniques. A table of all the films produced is given as Appendix A.

The laser energy density and beam area quoted in Appendix A are at the target surface where ablation occurs. The laser power is measured using a Coherent J4SLP-MUV-080 photodetector. The detector measures laser power outside the chamber at the entrance window, and at an exit window. This way, a good estimate of the transmission of the entrance window is made by the simple relation:

$$T = \sqrt{\frac{P_{exit}}{P_{entrance}}}. \tag{3}$$

Typically, the transmission coefficient is 0.9.

PLD is reported to result in films of identical stoichiometry to the targets from which they are ablated, and this has been used to analyze specific stoichiometries (Perkins *et al.* 2002a; Perkins *et al.* 2002b). However, there are also reports of film composition being different than that of the targets (Claeyssens *et al.* 2002).

In particular, ZnO targets are found to make films of zinc-to-oxygen ratios greater than unity. This is attributed to higher density plasmas created by high laser fluences and depositing in the absence of oxygen (Claeyssens *et al.* 2002). The high-density plasmas result in the re-deposition of the zinc onto the target, while the oxygen is evacuated from the system. Once the target's surface becomes richer in zinc, further ablation causes the film to be zinc rich as well. Unlike these reports, the ZTO films herein have generally been zinc deficient. This is explained in greater detail in Chapter 5.

3.3 Summary

PLD is a powerful tool to rapidly produce films. The electrical transport measurements did not provide continuous guidelines for the parameters under which transistor channel layers could be made. However, the results from the transport measurements give a good starting point, as well as a good idea of what the TTFTs' mobilities would be, based on the van der Pauw measurement results. This is described in greater detail in Chapter 5.

Chapter 4
CHARACTERIZATION TECHNIQUES

4.1 Introduction

The PLD system is used to produce two structures of films: transistor channel layers, and van der Pauw cross structures. The transistor channel layers are analyzed for transistor behavior and surface morphology by atomic force microscopy. All other characterization techniques are performed on the van der Pauw structures. This chapter reviews the methods used for the electrical transport measurements, optical characterization, compositional analysis, X-ray diffraction analysis, and atomic force microscopy.

4.2 Electrical Transport Measurements

The first films produced are intended to be conducting enough to measure electrical transport characteristics using a Lakeshore Hall Measurement System (HMS). For this, the films must have a resistance less than 20 MΩ across any two contacts to obtain accurate results for resistivity and Hall coefficient. Best results are obtained if indium contacts are soldered onto the film instead of pressure contacts. This reduces the noise in the measurements.

The HMS is configured to take resistivity and Hall voltage measurements in the van der Pauw geometry. The structure that is used for the measurements is shown in Figure 4.1.

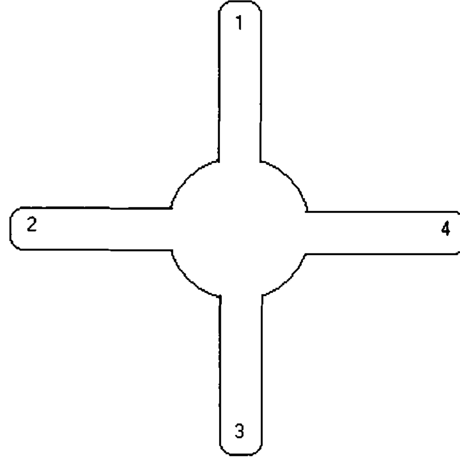

Figure 4.1: Structure for van der Pauw measurements. Contacts are labeled with the numbering convention used by the HMS.

For the measurements, the magnetic field B is applied perpendicular to the sample plane and a current is forced between two contacts while a voltage is measured across two separate contacts. To clarify, the following labeling convention is used: $V^{+}_{ij,kl}$ indicates a voltage measured across contacts k and l, while a positive current is sent from contact i to contact j. Resistivity is measured by the following equations that are found in the Lake Shore Hall Measurement System Manual (Lake Shore 1999).

$$\rho_A = \frac{\pi f_A t[\mathrm{m,cm}]}{\ln(2)}\left\{\frac{V^{+}_{12,43} - V^{-}_{12,43} + V^{+}_{23,14} - V^{-}_{23,14}}{I^{+}_{12} - I^{-}_{12} + I^{+}_{23} - I^{-}_{23}}\right\}[\Omega - \mathrm{m}, \Omega - \mathrm{cm}] \tag{4}$$

$$\rho_B = \frac{\pi f_B t[\mathrm{m,cm}]}{\ln(2)}\left\{\frac{V^{+}_{34,21} - V^{-}_{34,21} + V^{+}_{41,23} - V^{-}_{41,23}}{I^{+}_{34} - I^{-}_{34} + I^{+}_{41} - I^{-}_{41}}\right\}[\Omega - \mathrm{m}, \Omega - \mathrm{cm}] \tag{5}$$

In these equations, t is the film thickness. This method of resistivity differs from van der Pauw's method (van der Pauw 1958), but as long as the positive and negative voltage and current terms differ only by sign, then these give the same results as van der Pauw's resistivity equations. The resistivity is then an average

of ρ_A and ρ_B. f_A and f_B are geometrical factors, and are functions of geometrical resistance ratios, Q_A and Q_B, as shown below.

$$Q_A = \left(\frac{R^{+}_{12,43} - R^{-}_{12,43}}{R^{+}_{23,14} - R^{-}_{23,14}} \right) \tag{6}$$

$$Q_B = \left(\frac{R^{+}_{34,21} - R^{-}_{34,21}}{R^{+}_{41,23} - R^{-}_{41,23}} \right) \tag{7}$$

Here, $R^{+}_{ij,kl}$ indicates a resistance measured by V_{kl}/I_{ij}, where the voltage is measured across contacts k and j, while a positive current is sent from contact i to contact j. If either Q_A or Q_B is greater than one, then its reciprocal is used. f_N is determined by the following transcendental equation (Lake Shore 1999)

$$\frac{Q_N - 1}{Q_N + 1} = \frac{f_N}{\ln(2)} \cosh^{-1}\left\{ \frac{1}{2} \exp\left[\frac{\ln(2)}{f_N} \right] \right\}. \tag{8}$$

To measure Hall coefficient, the following equations are used.

$$R_{HC} = \frac{t[m]}{B[T]} \frac{V^{+}_{31,42}(+B) - V^{-}_{31,42}(+B) + V^{-}_{31,42}(-B) - V^{+}_{31,42}(-B)}{I^{+}_{31}(+B) - I^{-}_{31}(+B) + I^{-}_{31}(-B) - I^{+}_{31}(-B)} \left[m^3 - C^{-1} \right] \tag{9}$$

$$R_{HD} = \frac{t[m]}{B[T]} \frac{V^{+}_{42,13}(+B) - V^{-}_{42,13}(+B) + V^{-}_{42,13}(-B) - V^{+}_{42,13}(-B)}{I^{+}_{42}(+B) - I^{-}_{42}(+B) + I^{-}_{42}(-B) - I^{+}_{42}(-B)} \left[m^3 - C^{-1} \right]. \tag{10}$$

Here, t is the film thickness and B is the field intensity. The average Hall coefficient is then just a simple average of these two values. The sign of the Hall coefficient determines the type of the carriers in a material.

The Hall mobility is then calculated by (Lake Shore 1999)

$$\mu_H = \frac{|R_{Hav}|}{\rho_{av}} \left[m^2 - V^{-1} - s^{-1} \right]. \tag{11}$$

Another parameter to calculate is the carrier concentration, n. This is given by

$$n = \frac{1}{|R_{Hav}|q}, \tag{12}$$

where q is the charge of an electron. By convention, the symbol n is used for carrier concentration if the carriers are electrons, and p is used if the carriers are holes. ZTO, and most high conductivity TCOs are n-type, or electron carriers.

The HMS software calculated these values automatically, and the results were confirmed with calculations done by hand or using Excel.

4.3 Optical Characterization

Optical measurements are made using a grating spectrometer, described in detail in the senior theses of Levi Kilcher and Derek Tucker (Kilcher 2002; Tucker 2002). The spectrometer has a double monochromator to scan through wavelengths of light from 200 nm to 900 nm produced by a xenon or tungsten lamp, and focused onto the film. The intensity of the transmitted and reflected light is measured by a photodetector and recorded. From the transmission and reflection data, many useful properties are calculated, including the absorption coefficient (α) and the energy bandgap. The first quantities calculated are the transmission and reflection coefficients, T and R. These are calculated for all wavelengths by the following formulae:

$$T = \frac{I_{T(film+substrate)}}{I_{(lamp)}}, \quad R = \frac{I_{R(film+substrate)}}{I_{(lamp)}}. \tag{13}$$

With these values, a $\frac{T}{1-R}$ plot is made. This plot gives the transmission of the film, as it would be without interference fringes caused by interfaces of different refractive indices and thin-film geometry as well as eliminating the effects of

reflection. Also, with the $\frac{T}{1-R}$ data, a good approximation of the absorption coefficient, α, is made using the following formula (Hishikawa *et al.* 1991):

$$\exp(-\alpha d) = \frac{T}{1-R}, \tag{14}$$

where d is the thickness of the film.

The bandgap is estimated using the following relation (He *et al.* 2001):

$$\alpha E \propto \left(E - E_g\right)^r, \tag{15}$$

with $r = 1/2$ for direct bandgap crystalline semiconductors and $r = 2$ for amorphous semiconductors. In order to estimate the direct bandgap, a plot of $(\alpha E)^2$ versus the photon energy, E is made. The linear region of this plot associated with the onset of absorption is extrapolated to the energy axis. This value is a good approximation of the direct energy bandgap. For the indirect gap, a plot of $\sqrt{\alpha E}$ versus E is made and the same extrapolation is performed (He *et al.* 2001).

4.4 Compositional Analysis

For compositional analysis, two techniques, Electron Probe Microanalysis (EPMA) and Rutherford Backscattering (RBS) are used.

EPMA is a technique that analyzes for elemental composition. A beam of electrons of energies from 5 to 30 keV is focused on the surface of a sample to non-destructively ionize a small area (~ 5 μm) of the sample. This process induces characteristic X-ray emission by the elements in the sample. These X-rays are typically of energies from 0.1 to 15 keV. A standard sample of material is also analyzed along with the unknown, and the ratio of the emitted X-rays from the unknown to that of the standard is taken. This ratio, known as the raw *K*-ratio, is used to determine the relative concentration of a given material.

Generally, EPMA is used to determine the composition of bulk materials such as geological samples. For analyses of samples of homogeneous composition, the maximum X-ray penetration depth is around 1 mg-cm^{-2}, meaning that for a material with density of 10 g-cm^{-3}, the penetration depth is 1 μm (Pouchou, Pichoir 1999). This depth can vary by more than two orders of magnitude, depending on electron beam intensity and material density. In the case where the sample is a thin-film with thickness less than the ionization depth, the emitted X-rays from the substrate must be accounted for due to the diffusion of the electrons occurring mainly in the substrate. In order to model a thin-film for analysis by EPMA, a minimum of two measurements at different beam energies must be used: one at high energy such that the maximum ionization depth is greater than the film thickness, and the other at low energy such that the ionization depth is as close as possible to the film depth (Pouchou, Pichoir 1999). The STRATAgem software (SAMx 2003) for thin-film analysis is used to analyze the thin-film samples, and is based on the model given by Pouchou and Pichoir (Pouchou, Pichoir 1999).

For the films studied by EPMA, the relative concentrations of zinc, tin, and oxygen are analyzed. Since the films are deposited on SiO_2 substrates, analysis for oxygen content is not as accurate as for the zinc and tin due to oxygen being present in both film and substrate. Since the focus of the EPMA analysis is the zinc and tin ratios, this is not a serious issue. ZTO is electronically insulating and because of this, all films analyzed by EPMA must be coated with a conducting layer (~ 20 nm) of carbon to ground the surface for the prevention of surface-charge buildup. Studies are performed at the Center for Advanced Materials Characterization in Oregon (CAMCOR) located at the University of Oregon. The analyses are supervised by John Donovan.

Rutherford backscattering (RBS) is another technique that analyzes for composition. A beam of ions, usually helium, with energies of a few MeV is incident on the sample. The number and energy of the backscattered ions are recorded and used to gain information about the material composition as a function

of depth. The maximum detection depth is around 2 μm with a depth resolution of 2-30 nm (Exarhos 1993). The nominal beam size for RBS is 1 mm.

4.5 X-Ray Diffraction

X-ray diffraction (XRD) is used in thin-films to determine a specimen's composition and crystalline phases. A collimated, monochromatic beam of X rays of wavelength from 5 nm to 20 nm is incident on the sample at angle of theta to the surface. The incident beam is diffracted by the crystal planes according to Bragg's law,

$$\lambda = 2d\sin\theta \tag{16}$$

where d is the spacing between the planes. XRD generally produces a plot of the intensity of diffracted X rays versus the deviation angle, 2θ. This diffraction pattern is a unique fingerprint of the materials present. In the case of the films of this study, XRD is used to determine how the 600 °C anneal affected the films.

Measurements are taken by Paul Newhouse, using a Rigaku D/max-Rapid X ray spectrometer. A Cu K_α source is used to produce X rays with a wavelength of 1.5418 Å. The data are analyzed using the programs, AreaMax, MDIJ, and Crystal Clear.

4.6 Atomic Force Microscopy

Atomic force microscopy (AFM) is a technique used to determine the surface roughness of films. It is especially important that the films are smooth for use as channel layers in a layered TTFT. Films that are too rough result in poor electrical contact. To measure surface morphology, an atomically sharp silicon nitride stylus is scanned across the surface of the thin-film to detect relative depth variations.

For this project, a Digital Instruments MultiMode Scanning Probe Microscope is used in contact AFM mode. AFM measurements are taken by Robert Kykyneshi at Oregon State University.

The surface roughness is quantified by the root mean square roughness (*Rms*) and the arithmetic average roughness (*Ra*). These quantities are given by the equations,

$$Rms = \sqrt{\frac{\sum_{i=1}^{M}\sum_{j=1}^{M} Z^2(x_i, y_j)}{NM}} \tag{17}$$

$$Ra = \frac{\sum_{i=1}^{M}\sum_{j=1}^{M} Z_{ij}}{NM}, \tag{18}$$

where N and M are the number of points in x and y. Z_{ij} is the deviation of the ijth point from the mean plane.

4.7 Transistor Analysis

The transistor structures are tested using an HP 5156B Precision Semiconductor Parameter Analyzer to measure the source-drain current as the source voltage is varied at several different gate voltages. These measurements are carried out by David Hong and Matt Spiegelberg at Oregon State University. The source-drain current-voltage (I_{ds}-V_{ds}) characteristics produced are used to analyze channel mobility as described by Hoffman (Hoffman 2004). Optical measurements are made on representative transistor structures as well. More details about the analysis techniques and calculations used to characterize TTFTs can be found in Chapter 6.

Chapter 5
FILM CHARACTERIZATION RESULTS

5.1 Introduction

The results for the electrical transport measurements, optical characterization, compositional analysis, and X-ray diffraction analysis are given in this chapter. For the electrical transport measurements, most films are too insulating ($\rho \sim 100$ MΩ-cm) to be accurately measured by the Hall measurement system. For the films measured, the resistivity ranges from 1.73 Ω-cm to 251 MΩ-cm, and the Hall mobility range is from 1.6 to 10.4 cm^2-V^{-1}-s^{-1}. Optical measurements are carried out using a grating spectrometer. The films, in general, have transmittance over 80% in the center of the visible spectrum, roughly at 500 nm. The estimated bandgap ranges from 3.03 to 3.7 eV. Compositional analysis is performed using Electron Probe Microanalysis (EPMA) and Rutherford Backscattering (RBS). The deposited films consistently have less zinc than the targets by about 15%. X-ray diffraction (XRD) is carried out on one film before and after annealing in air at 600 °C. Preliminary conclusions from this analysis are that the annealing process causes the as-deposited amorphous films to remain primarily amorphous ZTO with the inclusion of some crystalline ZnO and a possibility of crystalline ZTO and SnO_2. Atomic Force Microscopy (AFM) is carried out on three different TTFT structures to analyze surface morphology. Root-mean squared roughness is calculated to be 9.6 nm for a film deposited at room temperature, 6.5 nm for a film deposited onto a substrate at 600 °C, and 4.7 nm for a film deposited at room temperature, followed by a 600 °C anneal in air.

5.2 Electrical Transport Measurement Results

For all films characterized using the Hall measurement system (HMS), a minimum of two consecutive runs are performed in order to gauge the drift and noise in the measurements. Since the resistivity and Hall coefficient are not observed to be field dependent, an average value for these is calculated using all field points. The resistivity (ρ), carrier concentration (*n*), and Hall mobility (*μ*) are plotted in Figure 5.1 for films deposited from the three different targets at varying oxygen deposition pressure.

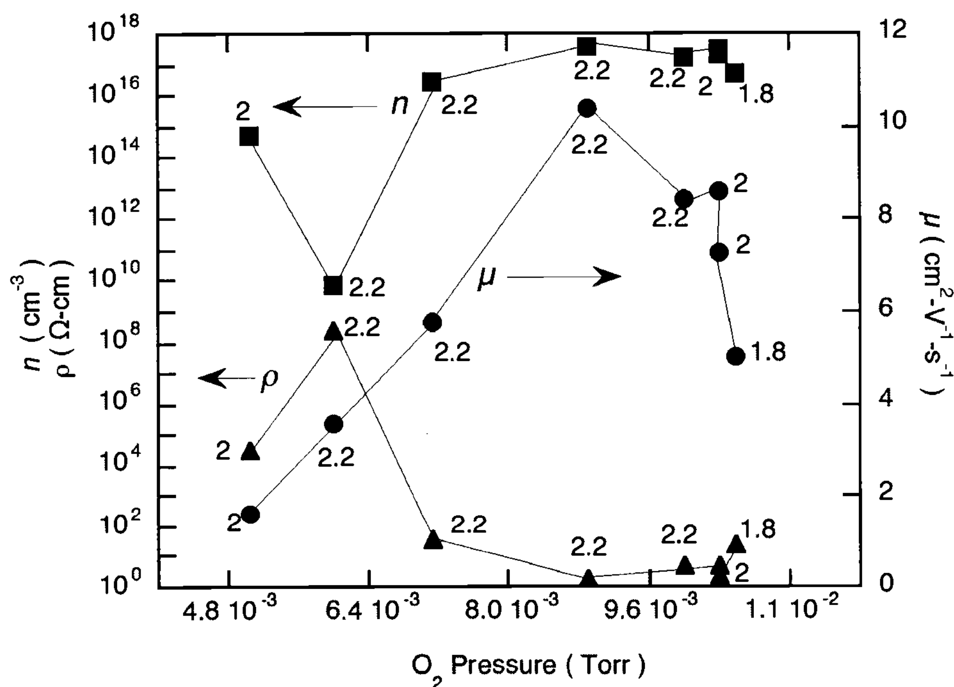

Figure 5.1: O_2 pressure during deposition for three different targets of $Zn_{(2-x)}Sn_xO_{(4+y)}$ labeled 2, 2.2, and 1.8.

In Figure 5.1, there is a maximum in mobility around 9 x 10^{-3} Torr deposition pressure. It also seems that the lower zinc-to-tin ratio targets result in lower mobilities, when observing the trend for films deposited at roughly the same O_2

pressure just above 1 x 10^{-2} Torr. The resistivity is very large for the films deposited at low pressure, and decreases with increasing pressure with a minimum around 9 x 10^{-3} Torr. The carrier concentration is inversely proportional to the resistivity with a maximum value of 3.54 x 10^{17} cm^{-3}.

The films all display *n*-type conductivity. The highest mobility for the ZTO films measured by the HMS is 10.4 cm^{2}-V^{-1}-s^{-1}. Carrier concentrations for the ZTO films are between 7 x 10^{9} and 3.54 x 10^{17} cm^{-3}. ZTO has reported carrier concentrations in the 10^{19} cm^{-3} range for crystalline films (Young 2000) and 10^{16} – 10^{19} cm^{-3} range for amorphous films (Young *et al.* 2002). The carrier concentrations measured are within the expected range for amorphous ZTO.

The parameter that has the largest effect on the resistivity is the deposition pressure. The highest resistivity values are obtained at the lowest deposition pressures (6 x 10^{-3} Torr) as seen in Figure 5.1, so this serves as the starting point for making transistor devices. This result of low oxygen pressure resulting in highly resistive films is anomalous, since oxygen vacancies are the usual source of conductivity in most TCOs.

These data from the van der Pauw measurements serve as a guide to the production of the first transistor channel layer films. Ideally, the transistor channel layer should be highly insulating, but have a high mobility when carriers are injected by applying a gate voltage as shown in Figure 5.2. High resistivity ($\rho >$ 100 MΩ-cm) is the most important parameter to ensure a working TTFT. This implies that the film has a low carrier concentration so that devices made from this material will have an 'off' state with very low conductivity, until carriers are injected by increasing the gate and drain voltages.

The first transistor channel layer is deposited at 6.98 x10^{-3} Torr, using the 2.2:1 target. This device is found to be too conducting (i.e.: had no 'off' state), despite the fact that the deposition parameters used are those that produce the most insulating film measured.

It is realized at this point that a channel layer that is insulating enough would probably have to be deposited under the conditions that produce films that are too

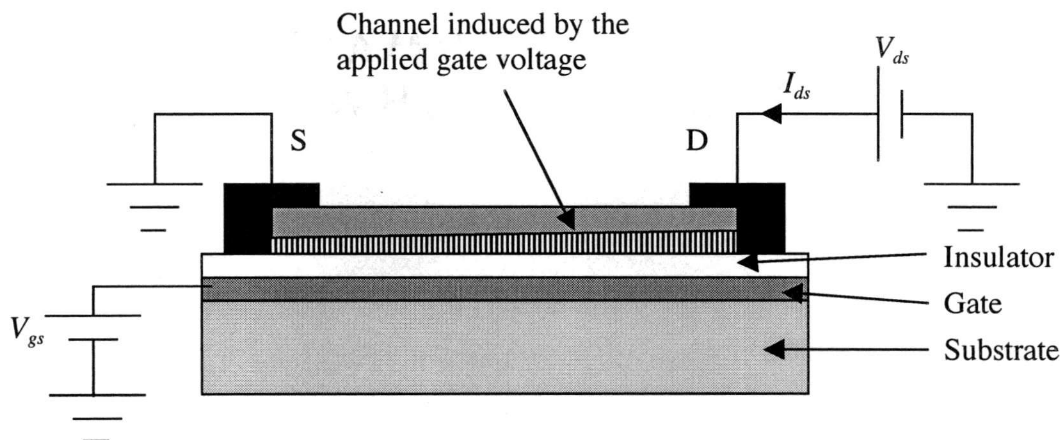

Figure 5.2: Enhancement-mode TFT showing conductive channel induced by a positive gate voltage. A positive drain voltage attracts channel electrons, resulting in a drain current, I_{ds}. Electron injection from the source to the channel supplies carriers to sustain I_{ds}.

insulating to even measure resistances using a multi-meter. It is not possible to characterize these highly insulating films using the HMS. For the transistors, it is found that a 600 °C anneal in air for 30 minutes produces the best transistor characteristics. After this realization, a Hall structure is deposited under the conditions that produce good transistor channel layers when annealed at 600 °C. This film is too resistive for characterization both before and after the anneal.

It is observed that the resistivities of the films change with ambient lighting. This observation leads to a simple experiment. Probes from a multi-meter are connected to contacts 1,3 on the film, and the film is covered with a cardboard box and left for a few hours. The room lights are then turned on and the box is removed. Resistance is recorded every 5 seconds. A second experiment is performed by doing the reverse. The film is left for a few hours with the room lights on, and then is covered. Again, resistance measurements are recorded every 5 seconds. The results of these two experiments are shown in Figure 5.3.

For the photoconductivity to be useful in a device such as a switch, the response time should be on the order of milliseconds. Here, it is on the order of minutes. A typical material used as a photoconductor is cadmium sulfide (CdS),

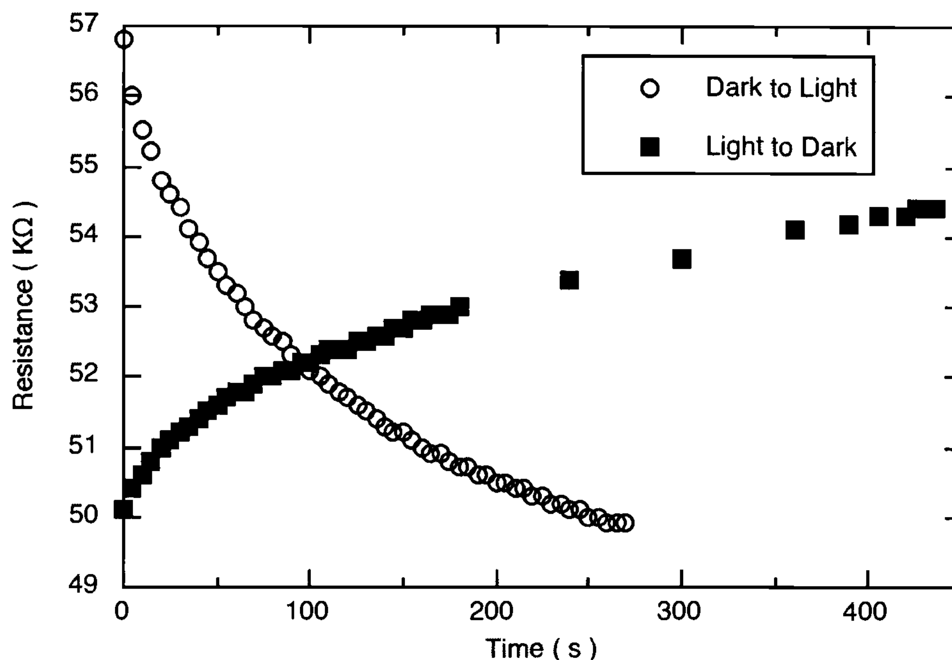

Figure 5.3: Photoresistance of Zn_2SnO_4. The resistance increases after a light source is removed, and decreases when a light source is applied. An interesting phenomenon, but the response time is too long for this to be useful in any application.

which has a typical rise times around 50 ms. The rise time of the ZTO sample tested is probably around 10 minutes, but the minimum resistance is never determined. This property is not examined further.

5.3 Optical Characterization Results

Plots of $\frac{T}{1-R}$ for films deposited from the three different target stoichiometries, at varying oxygen deposition pressures are shown in Figure 5.4.

The highest transmittance in the visible occurs for films deposited in higher oxygen pressures (oxygen pressures listed in Appendix A). The absorption

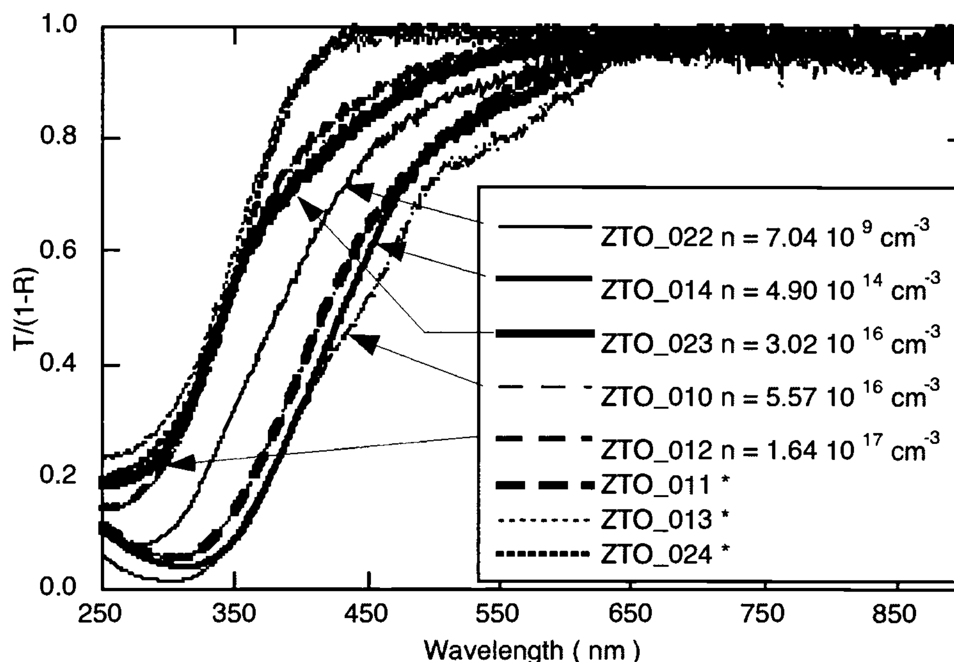

Figure 5.4: UV - visible (T/1-R) for various deposited films. Carrier concentrations are given, with '*' indicating films too insulating to measure carrier concentration.

coefficient for the films is calculated for all the wavelengths scanned. These data are plotted in Figure 5.5.

Next, the optical bandgap is estimated for the films. Analyses for both indirect and direct gaps are carried out. Bandgaps in amorphous semiconductors are not necessarily direct nor indirect since there is no well-defined *k* vector in amorphous materials. To determine the optical bandgap for amorphous semiconductors, He *et al* treat it as if it has an indirect bandgap (He *et al* 2001). However, when the analysis for the indirect bandgap is performed on these films, the results give very low energies (1.8 eV - 2.75 eV). With such small optical bandgaps, the films would not appear transparent.

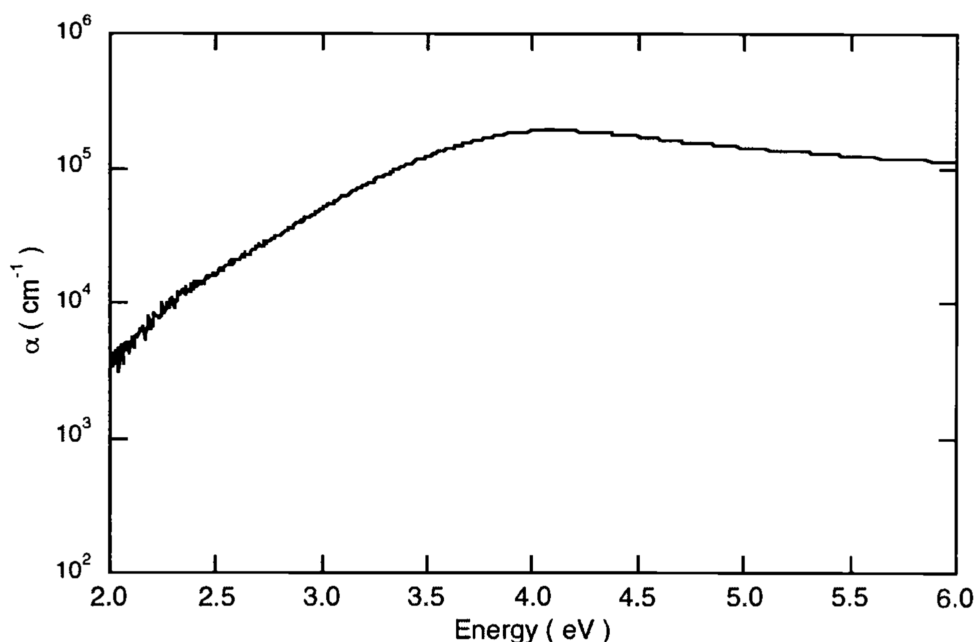

Figure 5.5: Absorption coefficient for a representative ZTO film. The energies plotted on the x-axis correspond to wavelengths from approximately 600 nm to 207 nm.

Analysis using the direct bandgap method, however, yields values close to that for the direct gap of crystalline ZTO, which is 3.35 eV (Young 2000). The bandgap analysis is represented for one of the films in Figure 5.6.

The optical bandgap analysis is carried out by extrapolating the linear region, which is associated with the onset of absorption, of the energy gap plot to the energy axis. The intercept is the energy for the indirect or direct gap, depending on the plot used. This onset of absorption can be seen in the absorption coefficient plot shown in Figure 5.7.

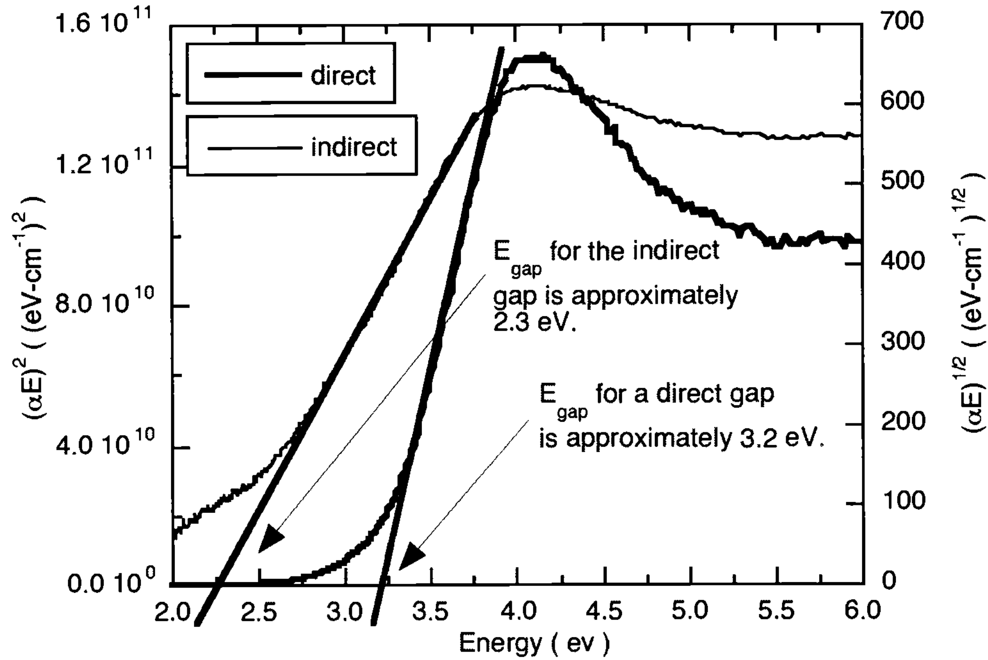

Figure 5.6: Bandgap analysis. Note the Urbach tail on the low energy sides of the absorption lines.

The exponential tail at the low energy side of the absorption edge is an Urbach tail (Urbach 1953), and is represented by (He *et al.* 2001):

$$\alpha(E) = \alpha_0 \exp\left[\frac{(E - E_0)}{\Delta E}\right], \tag{19}$$

with α_0 and E_0 being material dependent constants, and ΔE is a temperature dependent parameter that represents the width of the tail.

Results from all optical measurements for transmittance and absorption coefficient at 550 nm as well as the bandgap analyses are tabulated in Appendix B.

For most of the films deposited, the transmittance is exceptionally good, at greater than 80% at a wavelength of 500 nm. In general, the absorption coefficient is lower for films deposited in higher oxygen pressures.

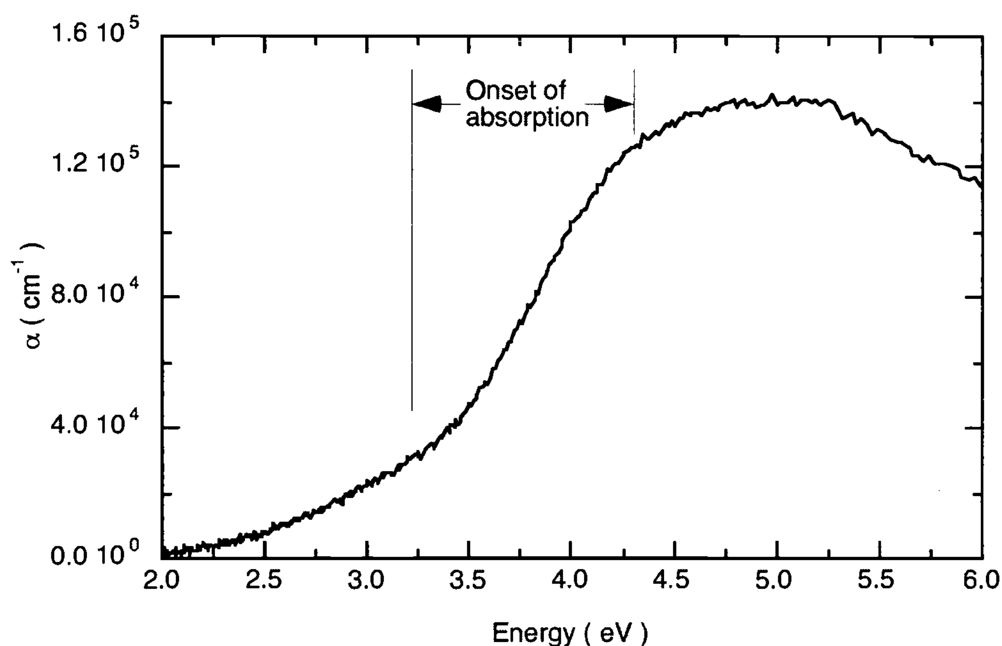

Figure 5.7: Absorption coefficient for ZTO_023 (Appendix A) showing the region of the onset of absorption. The corresponding region on the plot for bandgap approximation is extrapolated.

In Figure 5.8, the carrier concentrations are plotted against the optical bandgap energies for several films in order to observe the Burstein-Moss shift (Young 2000). The optical bandgap should increase with increasing carrier concentration due to carriers in the conduction band, which increase the optical bandgap, but not the fundamental bandgap. However, the variations in the optical bandgap do not confirm a Burstein-Moss shift.

Optical scans in the UV and visible are taken for some transistor structures as well. This is done after they are characterized as transistors. The results of these measurements are in Chapter 6 with all other transistor analyses.

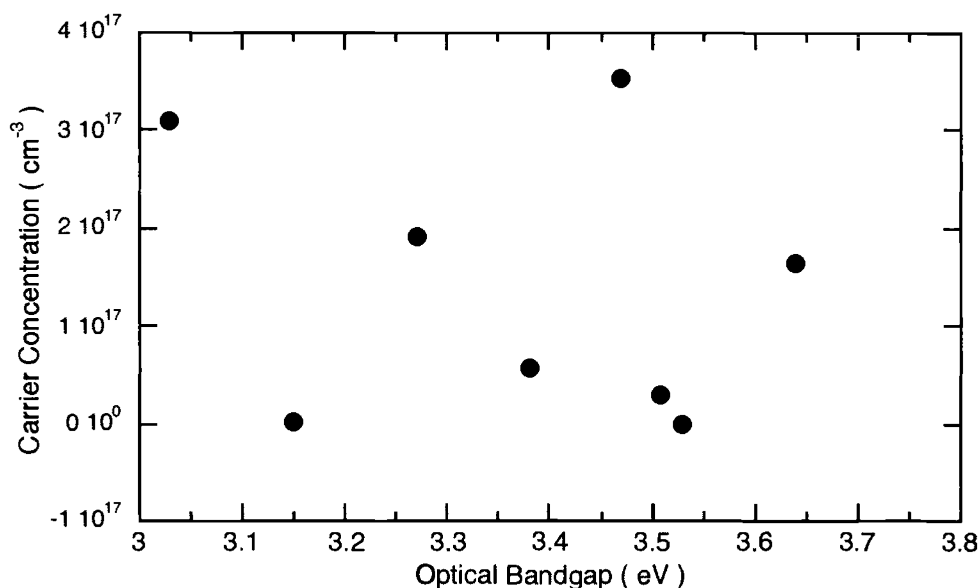

Figure 5.8: Carrier concentration versus bandgap energy for several ZTO films. The Burstein-Moss shift is not observed.

5.4 Compositional Analysis Results

EPMA is performed on films made from each target at various deposition pressures. The one consistent trend is that the percentage of zinc in the film is lower than that for the target. This is apparent in Figure 5.9, where the zinc-to-tin ratio obtained by EPMA and Rutherford Backscattering (RBS) for each film is plotted, along with the nominal zinc-to-tin ratio for the target from which each film was produced. The EPMA and RBS results agree to within 5% on average.

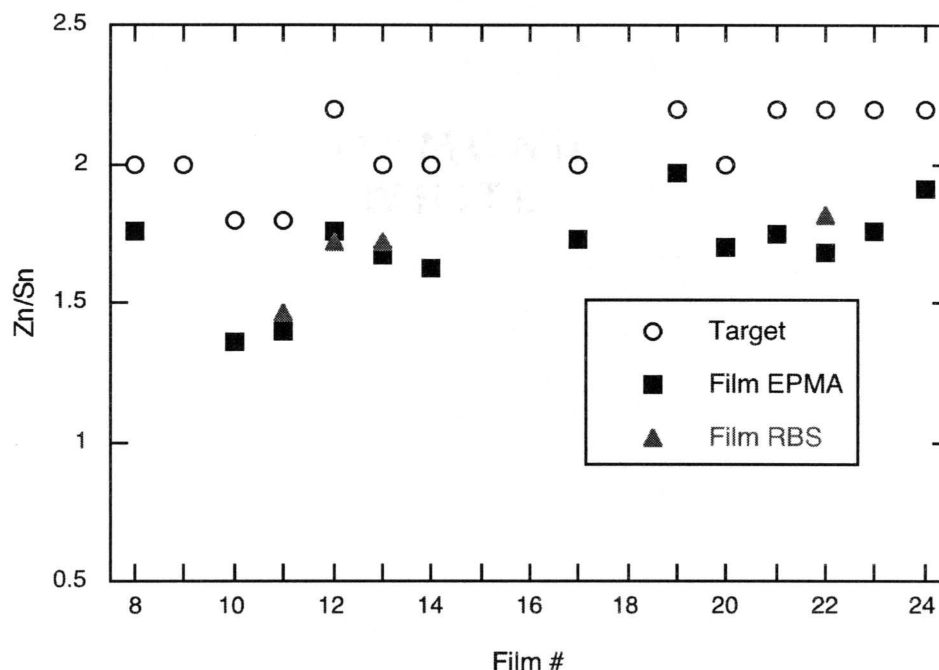

Figure 5.9: Zinc-to-tin ratios for all films measured. Circles give the nominal value for the target and squares represent the EPMA analysis for films. Triangles give the RBS values for films.

In order to further assess whether films are zinc deficient relative to the target, the targets are analyzed by with EPMA and this confirms that the target zinc-to-tin ratios are consistent with the intended stoichiometry, though the 1.8:1 target shows some phase separation as discussed later.

The targets are polished for the EPMA measurements, but the surfaces are not of uniform composition. The targets are examined by scanning electron microscopy (SEM). These SEM images are presented in Figures 5.10, 5.11, and 5.12 for the 2.0:1, 2.2:1 and 1.8:1 targets, respectively. Note the 20 μm marker scale in the left-hand side images in each.

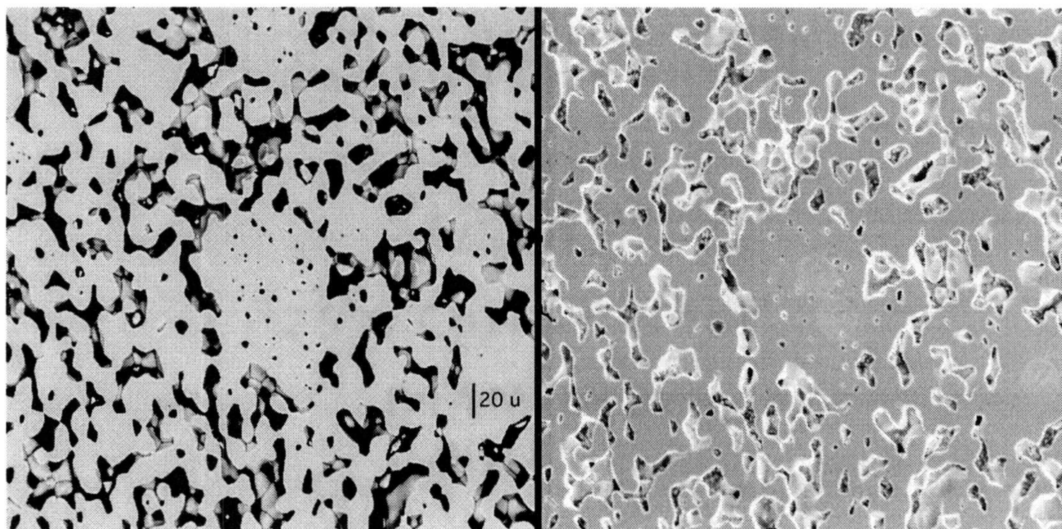

Figure 5.10: SEM images of the 2:1 target. The image on the left is from BSE mode, and the image on the right is from SE mode.

Figure 5.10 shows a portion of the 2:1 target. The left image is taken by operating in a mode that detects the backscattered electrons (BSE). This gives information about relative compositions. The image on the right is taken by operating in a mode that detects the secondary electrons (SE). In this image, the brighter intensities correspond to areas of higher slope. This gives surface morphology. The dark regions in the BSE image are 'holes' in the surface and not material of different composition. This is evident by comparison with the SE image. In the BSE image, the material itself (not the pits and holes) appears of the same intensity which means that the material is of uniform composition. This is expected, since the target was made on stoichiometry.

In the BSE image for the 2.2:1 target (Fig. 5.11), there is more compositional non-uniformity than in the 2:1 target. Besides the very dark regions that correspond to pitted areas as determined by their slopes in the SE image, there can be seen areas of slightly darker intensity grey. These are assumed to be ZnO rich regions. This non-uniformity can be resolved by EPMA if the electron beam size is on the same order as the size of the nonuniformities.

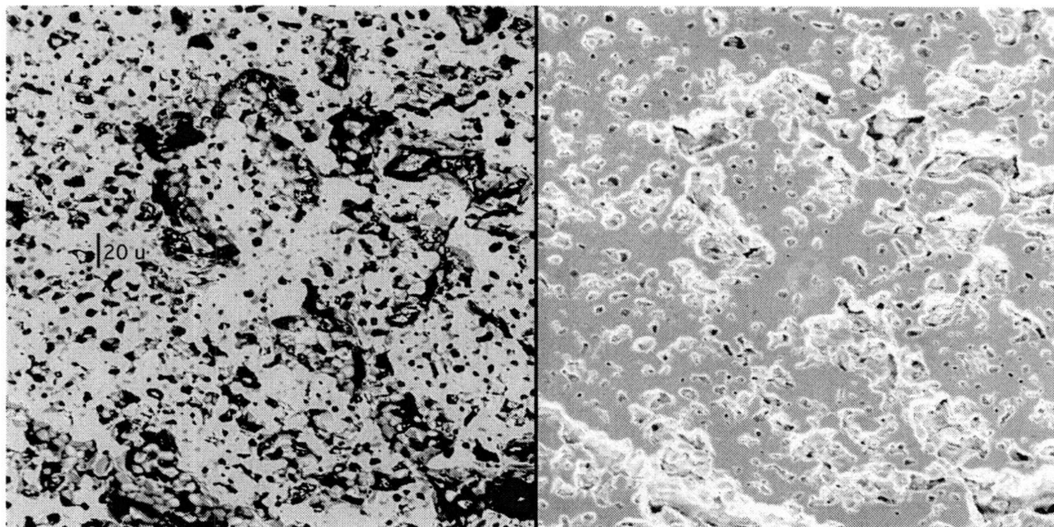

Figure 5.11: SEM images of the 2.2:1 target. The image on the left is from BSE mode, and the image on the right is from SE mode.

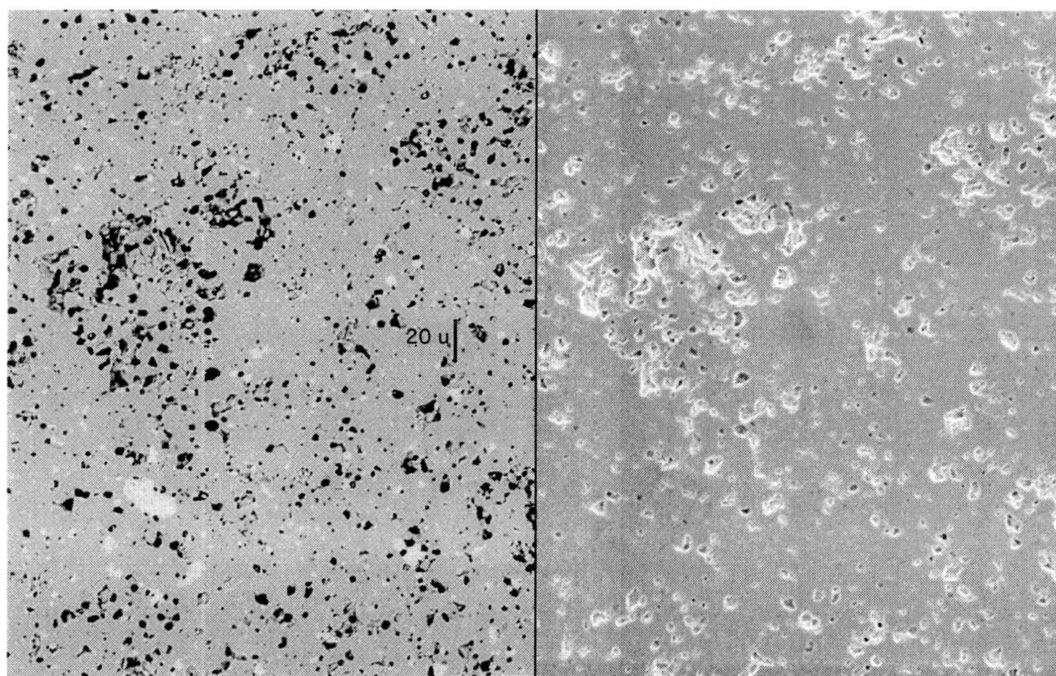

Figure 5.12: SEM images of the 1.8:1 target. The image on the left is from BSE mode, and the image on the right is from SE mode.

In Fig. 5.12, the BSE SEM image of the 1.8:1 target shows clearly resolvable regions of different composition. The lighter regions are determined by EPMA to be SnO_2. The size of the light regions in the BSE image is about equal to the electron beam diameter for EPMA of 4 μm. The results from EPMA reflect this resolvable non-uniformity. 12 random locations on the 1.8:1 target are used for analyses at beam voltages of 8, 14, and 20 kV. For each beam voltage, an average is taken of the 12 locations. These are presented for each target in Appendix C. For the 1.8:1 target, data are also taken using 5 locations within the bright regions only. This shows that the bright regions are mostly SnO_2.

The errors for each target are calculated to be 6.5% for the 1.8:1 target, 2.4% for the 2:1 target, and 0.73% for the 2.2:1 target. The percent error for the 1.8:1 target is high due to the first two data points. In these instances, the beam is probably focused on a disproportionate number of regions with the 2:1 relative stoichiometry, and misses the areas of high SnO_2 concentration. After examining these EPMA data for the targets, it is confirmed that the nominal stoichiometries are correct. The off-stoichiometry targets have phase separated, as confirmed by SEM and EPMA. This phase separation leads to inconsistent data from EPMA since the small number of beam locations may not reflect an average over the entire target. The conclusion from this is that the targets are of the intended stoichiometry, and are not the cause of the films' zinc deficiencies.

The next parameter that is examined in the search for controlling zinc content in films is the laser pulse energy density. It is reported that high energy densities for PLD of thin-films of ZnO result in higher Zn concentrations when deposited in vacuum (Claeyssens *et al.* 2002). The zinc-to-tin ratios versus the energy density and oxygen deposition pressure are examined in Figures 5.13 and 5.14 for the ZTO films of this study.

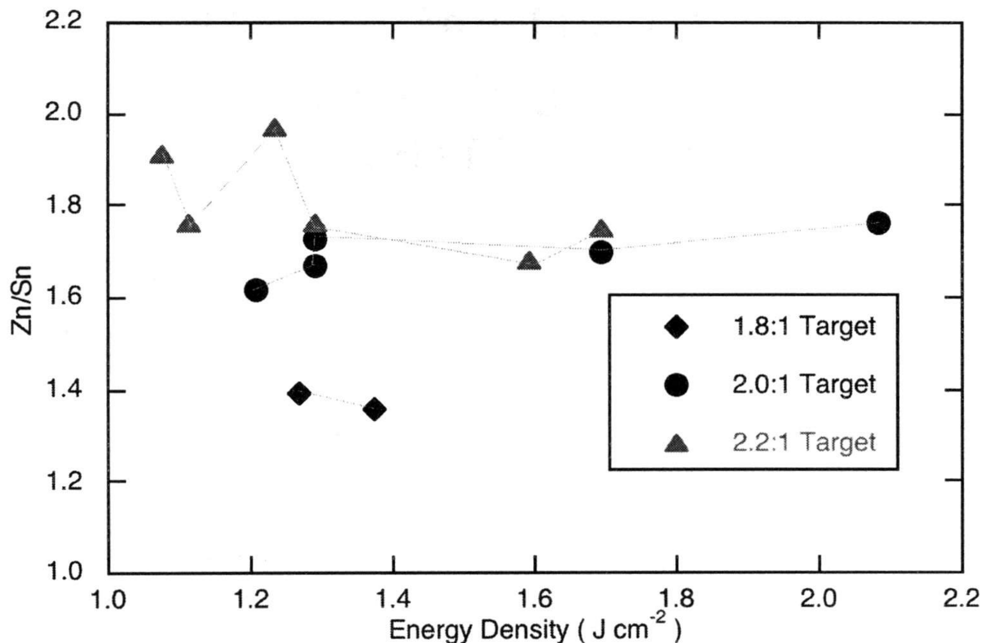

Figure 5.13: Zinc-to-tin ratios for films of three targets deposited at varying laser pulse energy densities. Oxygen deposition pressures in Torr are listed for each data point.

In Figure 5.13, the energy density has a very minor effect on the films' zinc-to-tin ratios. In Figure 5.14, there is no obvious effect on zinc-to-tin ratio by oxygen deposition pressure. Note that Claeyssens's result of zinc rich films takes the ratio of zinc to oxygen for ZnO films, and that the zinc deficient films reported herein are not in contradiction with Claeyssens's result, since the material system is different. However, in both cases, non-stoichiometric transfer is observed for PLD under given deposition conditions.

Four of the ZTO films are analyzed using RBS by Thin-film Analysis, Inc. located in San Jose, CA. The results obtained agree to within 5% with results from EPMA. Unlike EPMA, RBS gives composition data as a function of sample depth. In Figure 5.15, this depth profile is shown for one of the films characterized by RBS. The 20 nm layer of carbon over the sample is from the EPMA characterization.

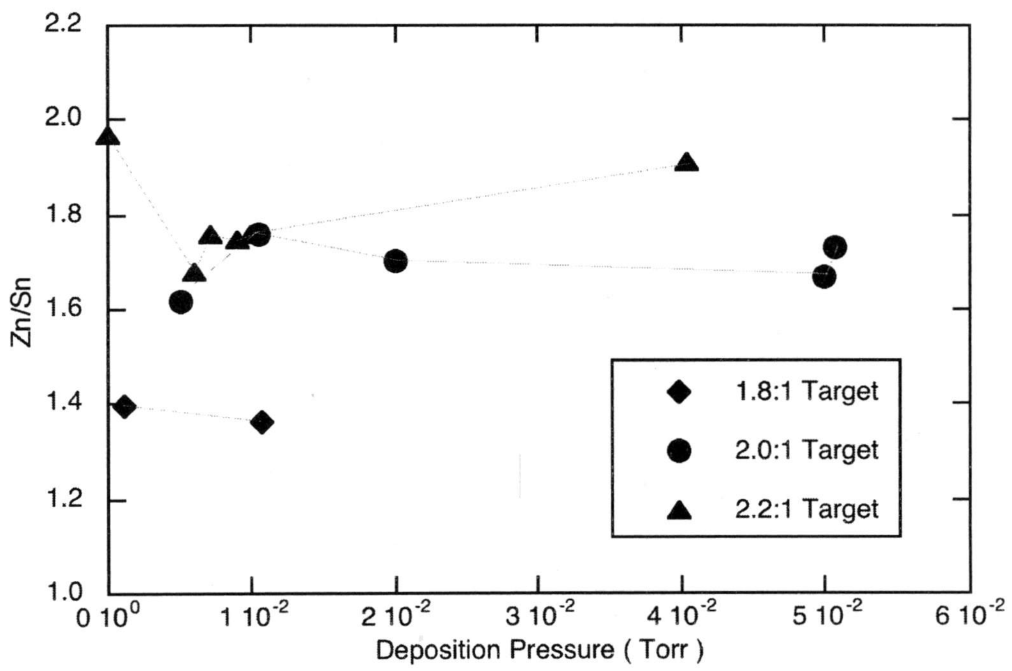

Figure 5.14: Zinc-to-tin ratio versus oxygen deposition pressure for films ablated from three different targets. All films were deposited at room temperature.

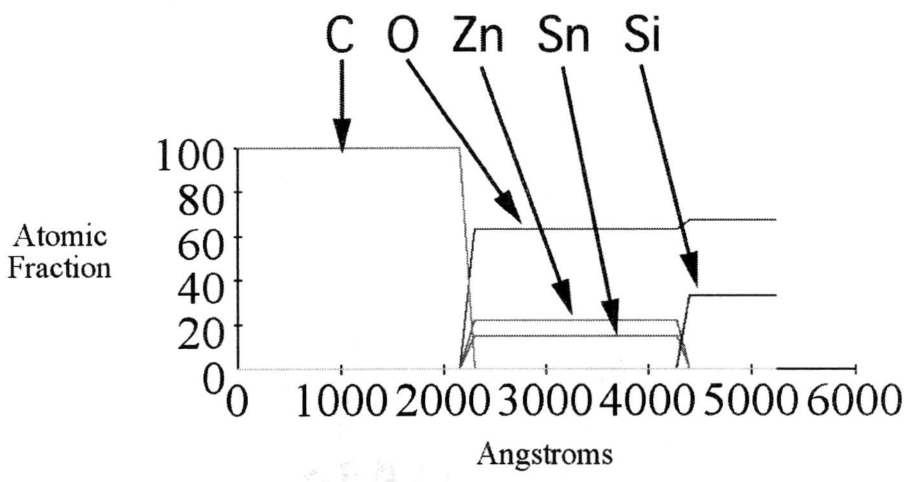

Figure 5.15: Depth profile for film ZTO_011 analyzed by RBS. The surface is at position 0.

The RBS analysis shows that the films produced have less zinc than the targets. This confirms the EPMA results. RBS results are tabulated in Table 5.1.

Film #	Zn:Sn RBS	Zn:Sn EPMA	% difference
ZTO_011	1.467	1.39	5.5
ZTO_012	1.724	1.76	2.0
ZTO_013	1.724	1.67	3.2
ZTO_022	1.818	1.68	8.2

Table 5.1: RBS results for the zinc-to-tin ratios compared with the EPMA results.

The difference between RBS and EPMA is less than 5%, on average. For deposition conditions of the films listed, see Appendix A.

5.5 X-Ray Diffraction Analysis Results

The transistors made with ZTO channel layers from the 1.8:1 target show improved I_{ds}-V_{ds} behavior and higher mobilities after being annealed at 600 °C in air for about 30 minutes. A film from this target is selected for XRD analysis. First, an XRD analysis is performed on the film before annealing. Then, the film is annealed in air at 600 °C for 30 minutes and left to cool slowly for about 6 hours, and the XRD analysis is repeated. The results for both analyses are shown in Figure 5.16.

For this analysis, the substrate spectrum is taken and subtracted from the scan. The broad peak in the as-deposited film's spectrum is indicative of short-range order. Amorphous glass exhibits the same characteristic. The same broad peak appears in the annealed film's pattern, indicating that amorphous material is still present.

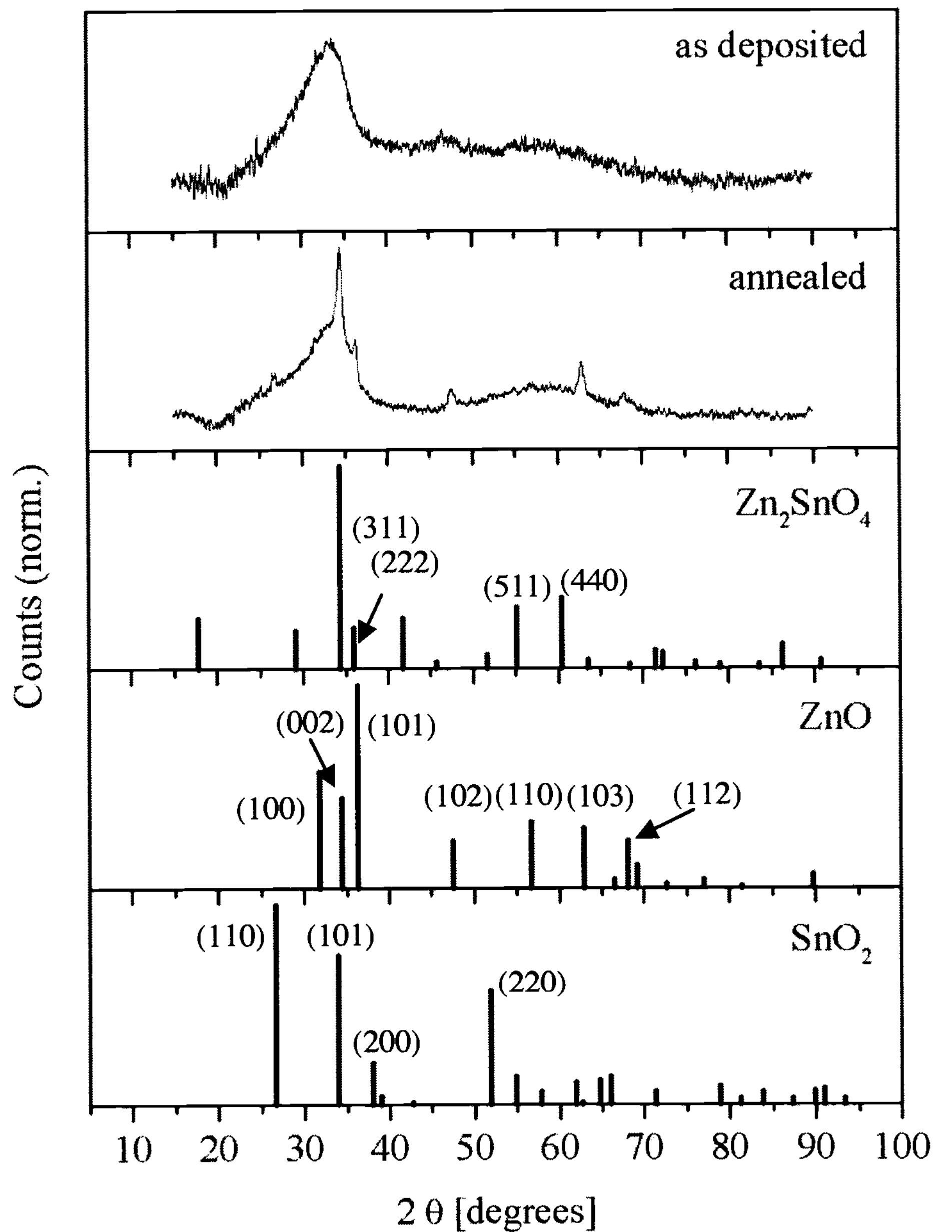

Figure 5.16: XRD analysis of film ZTO_044 before and after annealing. The lower three plots are from the JCPDS powder diffraction file database with significant peaks labeled by (h,k,l) lattice parameters.

Peaks are compared to those produced from XRD analysis on powders of Zn_2SnO_4, ZnO, and SnO_2 from the JCPDS powder diffraction file database. These peaks from powders show peaks with (h,k,l) lattice parameters for all possible crystal orientations. In the case of polycrystalline films with preferred orientation, not all these peaks would appear, and the relative intensities of the peaks would not necessarily match those from the JCPDS files.

The best interpretation of the XRD pattern of the annealed films is that it is primarily amorphous ZTO with nanocrystalline inclusions of ZnO and the possibility of nanocrystalline inclusions of SnO_2 and Zn_2SnO_4.

The case for crystalline ZnO is made by the appearance of peaks in the annealed film spectrum which line up well with the (002), (101), (102), and (103) peaks in the ZnO powder spectrum, as well as a broad peak near 67 degrees 2Θ which can be attributed to the three peaks in the ZnO powder spectrum in that location. There is a possibility that some ZTO is crystallized, evidenced by the (311) and (222) peaks, as well as a small peak in the location of the (511) peak in the powder spectrum. The ZTO (311) and (222) peaks are close to the ZnO (002) and (101) peaks, so the presence of crystalline ZTO is inconclusive. Crystalline SnO_2 may be present by the appearance of a small peak at the SnO_2 powder file's (110) peak location. However, no other peaks in the annealed film spectrum line up with peaks in the SnO_2 powder spectrum.

The lack of quantitative agreement between the intensities of the XRD pattern and the intensities listed for the ZTO, ZnO, SnO_2 powder patterns may be related to preferred orientation of polycrystalline grains in the film. This phenomenon is common in thin-films, but is usually more pronounced for more anisotropic materials.

From this XRD analysis, a preliminary conclusion is that the annealed film contains some crystalline phases of ZnO in a predominately amorphous ZTO bulk. It is reported that 600 °C is not a high enough temperature to cause ZTO to become crystalline (Chiang *et al.* 2004; Park 2004). At this annealing temperature,

though, it is possible for crystalline ZnO to form (Park 2004), and this is observed in the XRD pattern.

5.6 Atomic Force Microscopy

For atomic force microscopy (AFM), surface maps showing morphology are generated. From these, an estimation of grain size can be made, as well as calculations for surface roughness. Three transistor devices are tested using AFM. One device is tested as-deposited (ZTO_045B), another after the 600 °C anneal (ZTO_045A), and one that has been deposited onto a heated substrate at 600 °C (ZTO_046). Also, an analysis of the ATO (top layer of substrate) is performed for each sample. In Figure 5.17, the surface maps are shown for the three devices tested.

The top left image in Figure 5.17 shows the surface of ZTO_045B, which is deposited at ambient temperature, and not annealed. The grains are not well defined, as would be expected from amorphous material. The next image at the top right of Figure 5.17 shows the surface of ZTO_045A, which is annealed at 600 °C in air following deposition. This image shows some poorly defined grains about 200 nm across. The bottom left image is of ZTO_046, which is deposited in oxygen onto a substrate heated to 600 °C. The grain size is around 100 nm, and the grains are even more defined. The last image at the bottom right is of the substrate (ATO) for ZTO_046. This image shows clear grains that range in size from 100 – 200 nm.

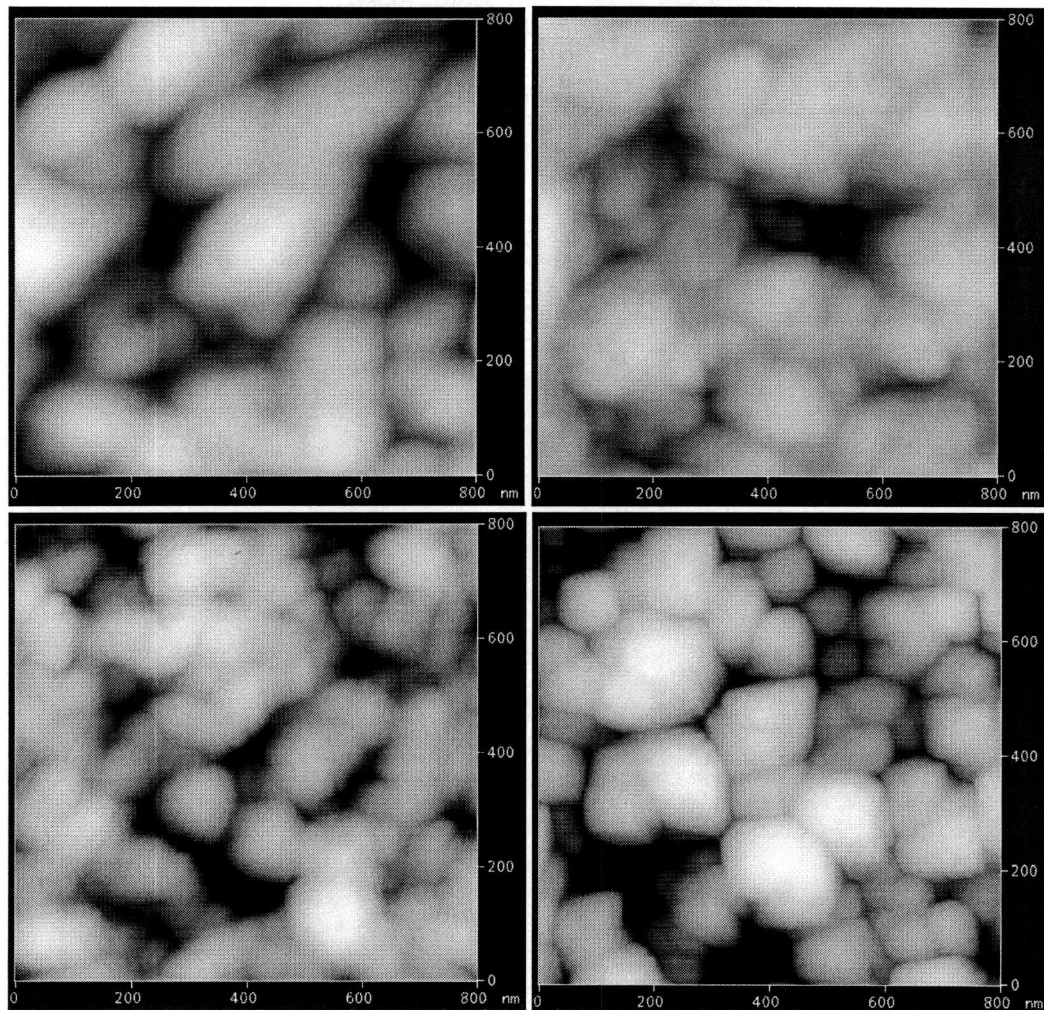

Figure 5.17: AFM surface roughness maps. Top left shows ZTO_045B, top right is ZTO_045A, bottom left is ZTO_046, and bottom right is the ATO layer from ZTO_045B.

The root-mean-squared (*Rms*) roughness and average roughness (*Ra*) are calculated. The results show that the film annealed at 600 °C is the smoothest film, with an average roughness of 3.8 nm, and the as-deposited film is the least smooth, with an average roughness of 7.8 nm. The variation in the ATO surface roughness is minor, but the 600 °C deposit seems to affect this ATO layer by making it slightly rougher than the other substrates. The as-deposited ZTO has greater surface roughness than the substrate. For heated processes, the deposited films are smoother than the ATO layer onto which they are deposited, which is

advantageous for devices such as TTFTs, where smooth interfaces are desired for source, drain, and gate contacts. Further experiments must be carried out to make generalizations about the effect of the annealing process on surface roughness.

5.7 Summary

The results for the electrical transport measurements, optical characterization, compositional analysis, and X-ray diffraction analysis have been given. For the electrical transport measurements, most films are too insulating ($\rho \sim 100$ MΩ-cm) to be accurately measured by the Hall measurement system. Since none of these films are annealed, they are amorphous as determined by XRD. For the films measured, the resistivity ranges from 1.73 Ω-cm to 251 MΩ-cm, and the Hall mobility range is from 1.6 to 10.4 cm^2-V^{-1}-s^{-1}. The films, in general, have transmittance over 80% in the center of the visible spectrum, roughly at 500 nm. The estimated bandgap ranges from 3.03 to 3.7 eV, which encompasses the fundamental bandgap for crystalline ZTO, which is 3.35 eV (Young 2000). Electron Probe Microanalysis (EPMA) and Rutherford Backscattering (RBS) results show that the deposited films consistently have less zinc than the targets by about 15%. X-ray diffraction (XRD) is carried out on one film before and after annealing in air at 600 °C. Preliminary conclusions from this analysis are that the annealing process causes the as-deposited amorphous films to remain predominately amorphous ZTO with the inclusion of nanocrystalline ZnO and possibly some crystalline ZTO and SnO_2. Atomic Force Microscopy (AFM) is carried out on 3 TTFT structures to analyze surface morphology. Root-mean squared roughness is calculated to be 9.6 nm for a film deposited at room temperature, 6.5 nm for a film deposited onto a substrate at 600 °C, and 4.7 nm for a film deposited at room temperature, followed by a 600 °C anneal in air.

Chapter 6
TRANSPARENT THIN-FILM TRANSISTORS

6.1 Introduction

This chapter gives an overview of the calculations used in analyzing TFTs, and results of the analyses. The most effective processing parameter in manufacturing high quality TTFTs is a post-deposition anneal at 600 °C in air. The next most effective processing parameter is the oxygen deposition pressure. Target zinc-to-tin ratio had a minor effect on device performance. Maximum average and incremental mobilities are 8.4 and 6.6 cm^2-V^{-1}-s^{-1} for the best device. It is found that after time, the transistors degrade due to surface absorption of gasses and other impurities in the channel layer. This creates an additional path in the surface of the film in which carriers can travel. If this surface channel is more conducting than the bulk, then control of the channel's conductivity via gate voltage is lost. The degraded channel layers can be improved by a low temperature (100 °C) anneal, which is believed to cause the absorbed impurities to desorb from the film.

For reference, a (TFT) test structure is shown in Figure 6.1. Two types of TFTs are enhancement-mode and depletion-mode. Enhancement-mode devices conduct negligible source-drain current in the absence of gate voltage. As gate voltage is applied, charge is injected from the source electrode into the channel layer, enhancing its conductivity. Depletion-mode devices have conducting channel layers at zero gate bias that are made more or less conducting when a gate bias of appropriate polarity is applied. More discussion about field-effect devices can be found in Pierret (Pierret 1996).

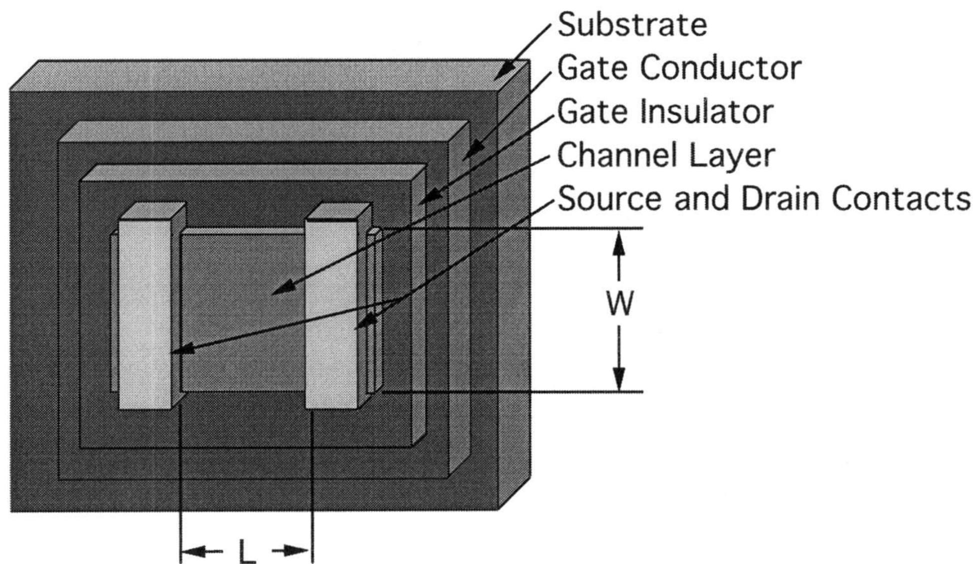

Figure 6.1: TFT test structure.

The square-law relationship describing the source-drain current (I_{ds}) in terms of the drain-source voltage (V_{ds}) and gate-source voltage (V_{gs}) is (Pierret 1996)

$$I_{ds} = \frac{W}{L} C_{ox} \mu \left[\left(V_{gs} - V_t \right) V_{ds} - \frac{V_{ds}^2}{2} \right], \tag{19}$$

where W and L are the channel layer's width and length as shown in Figure 6.1, C_{ox} is the capacitance of the insulating oxide layer, μ is the channel mobility, and V_t is the threshold voltage. This equation describes the parabolic nature of the I_{ds} versus V_{ds} (I_{ds}-V_{ds}) curves at low V_{ds}. This does not describe the saturation aspects. This I-V relation is sketched in Figure 6.2 for a typical enhancement-mode transistor.

In the theoretical I_{ds}-V_{ds} plot shown, the transistor is off at $V_{gs} = 0$ V, and displays a 'hard' saturation at each gate voltage tested. Hard saturation is designated as the portion of the curve in which I_{ds} is constant with increasing V_{ds}. Many inferior transistors continue to have slowly increasing drain current as the drain voltage is increased. This behavior is denoted 'soft' saturation.

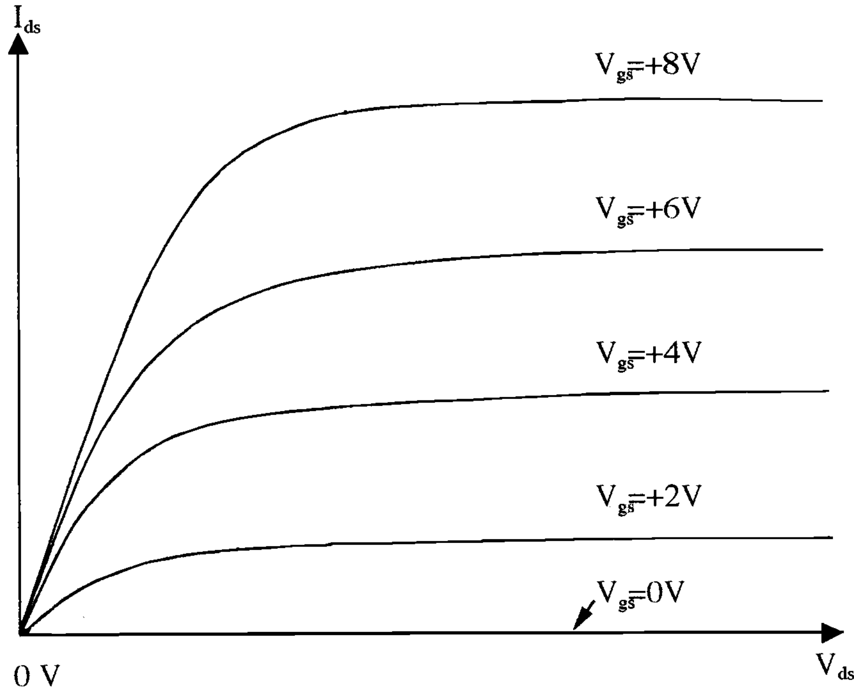

Figure 6.2: Theoretical I_{ds}-V_{ds} curves for a typical enhancement-mode transistor. To the left is the I_{ds} versus V_{gs} characteristic, which defines the saturation drain voltage.

To characterize the transistor, the quantities mobility and drain current on-to-off ratio are determined. Two types of mobility, incremental and average, are defined (Hoffman 2004). These are determined by using the I_{ds}-V_{ds} characteristics to calculate the channel conductance. The channel conductance is defined by

$$G_{CH}(V_{GS}) \equiv \lim_{V_{DS}\to 0}\left(\left.\frac{\partial I_{DS}}{\partial V_{DS}}\right|_{V_{GS}}\right) \cong \left.\left(\left.\frac{\Delta I_{DS}}{\Delta V_{DS}}\right|_{V_{GS}}\right)\right|_{small\ \ V_{DS}} . \tag{20}$$

To extract the average mobility from the channel conductance, the expression

$$\mu_{avg}(V_{GS}) = \frac{G_{CH}(V_{GS})}{\frac{W}{L}C_{ox}\left[V_{GS} - V_{on}\right]} \tag{21}$$

is used. W and L are the channel width and channel length, and C_{ox} is the capacitance of the gate insulator. V_{on} is the turn-on voltage of the transistor. V_{on} is defined as the applied gate voltage which results in a sharp increase in I_{ds}. This quantity is found from a plot of log(I_{ds}) versus V_{gs}. The average mobility differs from the oft-reported effective mobility by use of V_{on} in place of the threshold voltage. The incremental mobility is calculated by

$$\mu_{inc}(V_{GS}) = \frac{\frac{\Delta G_{CH}}{\Delta V_{GS}}}{\frac{W}{L}C_{ox}}. \tag{22}$$

The drain current on-to-off ratio ($I_{on:off}$) is defined as the maximum difference of I_{ds} at two different gate voltages. The final parameters to consider are the optical transmittance and surface roughness. For TTFTs, the optical transmittance should at least 80% in the visible range (roughly 400-700 nm).

6.2 Device Manufacture and Testing

TTFTs are made by depositing ZTO channel layers onto ATO/ITO/Glass substrates provided by Planar Systems. Aluminum source and drain contacts, about 200 nm thick, are evaporated onto the channel layer. Next, contacts are made to the gate layer by scratching through the ATO layer and soldering indium to the ITO layer. After all the necessary contacts are made, the sample is analyzed using an HP 5156B Precision Semiconductor Parameter Analyzer. The source-drain voltage (V_{ds}) is varied from 0 to 40 V in 1-V increments for varying gate voltages. The source-drain current (I_{ds}) is measured and recorded. The range for the gate voltages used depends on the performance of the transistor structure. If the transistor structure displays no transistor characteristics, which is obvious early

in testing, then a few gate voltages such as 0 to 40 V in 10 V increments are enough to show that the device is not a good transistor. For devices that show promising transistor behavior, increments of 1 V are used for the gate voltage. David Hong and Matt Spiegelberg from the School of Electrical Engineering and Computer Science at Oregon State University carried out these transistor measurements.

The I_{ds} vs. V_{ds} data are plotted to show the test structure's transistor behavior, if there exists any. These I_{ds}-V_{ds} curves are sketched for transistor ZTO_038 (deposition conditions are given in Appendix A) in Figure 6.3.

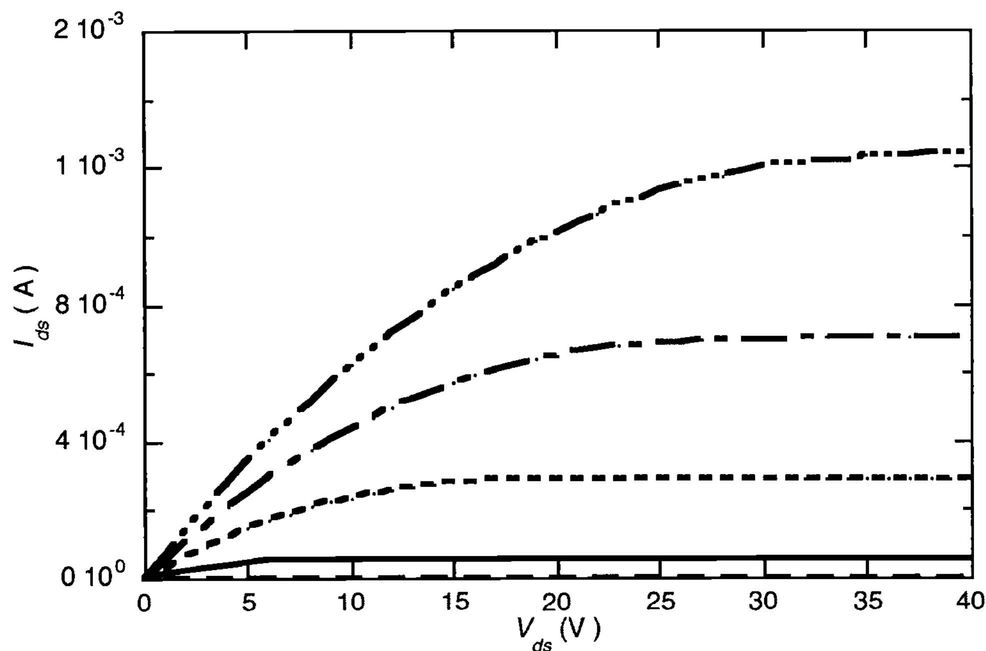

Figure 6.3: I_{ds}-V_{ds} characteristics for transistor ZTO_038 (Appendix A). Each curve corresponds to a 10 V increment in gate voltage, with the bottom curve being at V_{gs} = 0 V and the top curve at V_{gs} = 0 V.

To determine V_{on}, a plot of log(I_{ds}) vs. V_{gs} (transfer curve) is made as indicated in Figure 6.4. The turn-on voltage is defined as the gate voltage that corresponds to an abrupt increase in the drain current.

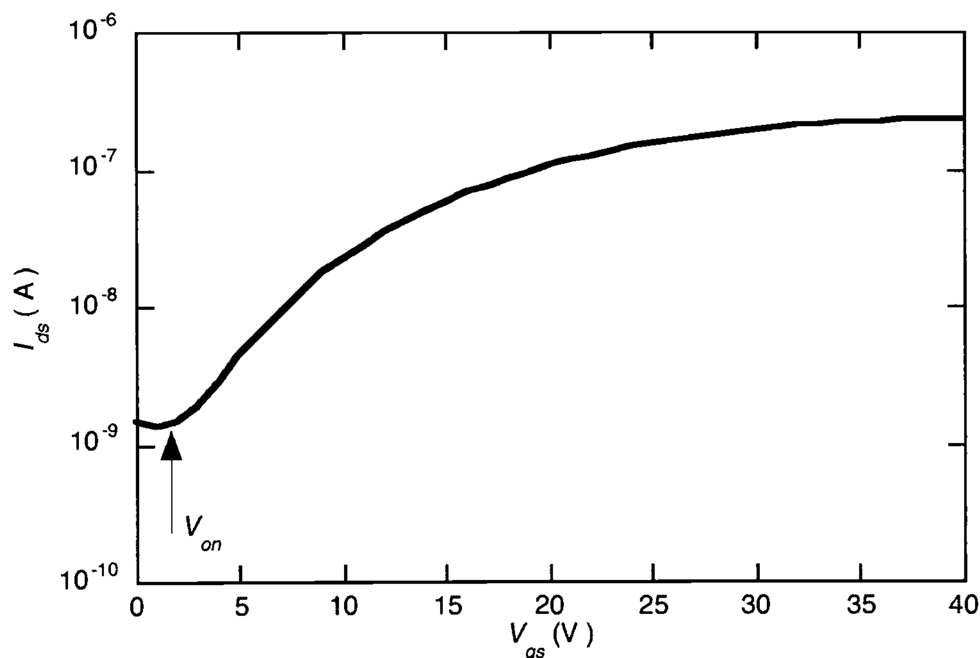

Figure 6.4: Transfer curve for transistor ZTO_042 (Appendix A). This plot is used to determine the turn-on voltage for the channel layer.

In the case presented above, V_{on} is 3 V.

6.3 Results and Discussion

For each of the three targets, three films are deposited at varying deposition pressures. Pressures used are roughly 6 x 10^{-2} Torr (high pressure), 6 x 10^{-3} (medium pressure) and "vacuum" depositions in which no oxygen is admitted into the deposition chamber. For the vacuum depositions, the base pressure is around 10^{-8} Torr, but during depositions, the chamber pressure fluctuates between 10^{-6} Torr and 10^{-7} Torr ranges. Several films are annealed in a Barnstead Thermolyne 62700 furnace at either 300 °C or 600 °C in air to improve device performance. Annealing of the films is done by David Hong, Matt Spiegelberg, and Rick Presley. After each film is deposited (and annealed if applicable), aluminum source and drain contacts are deposited, and the film is tested for transistor

behavior. $I_{on:off}$, and the incremental and average mobilities are used to characterize the devices. These values are tabulated and shown in Appendix D. Device performance is observed to degrade after time stored in ambient laboratory conditions. This is evident in the two sets of I_{ds}-V_{ds} curves for ZTO_045A (Appendix A) shown in Figure 6.5.

The first analysis of the device shows hard saturation with a current drive of about 1.6 mA at the gate voltage of 40 V. The second analysis, performed three days later, shows that gate control is being lost. The device starts to show a superposition of variable resistor behavior and transistor behavior. Notice also that the current drive for the V_{gs} curve is about ten times lower for a given gate voltage in the second analysis than in the first analysis.

Device ZTO_043 (Appendix A) also displays non-ideal behavior after storage in ambient conditions. Immediately after manufacture, this device displays ideal I_{ds}-V_{ds} characteristics similar to those for ZTO_045A with a current drive of 1.5 mA at a 40 V gate voltage and a turn-on voltage of approximately –2 V. After two weeks of storage, highly non-ideal behavior is observed which is difficult to model. After a few months of storage, this device is annealed at 100 °C, at which point ideal I_{ds}-V_{ds} characteristics return. It is then stored again for another week, and the test is repeated. The resulting I_{ds}-V_{ds} characteristics for these two analyses are shown in Figure 6.6.

The degradation shown in the I_{ds}-V_{ds} plot in Figure 6.6 shows that the device is beginning to lose gate modulated hard saturation. The current drive also increases after the week of storage. The turn-on voltage also drops from around –2 V for this device, when tested roughly two months before this experiment, to below –10 V after the anneal, becoming more depletion-mode.

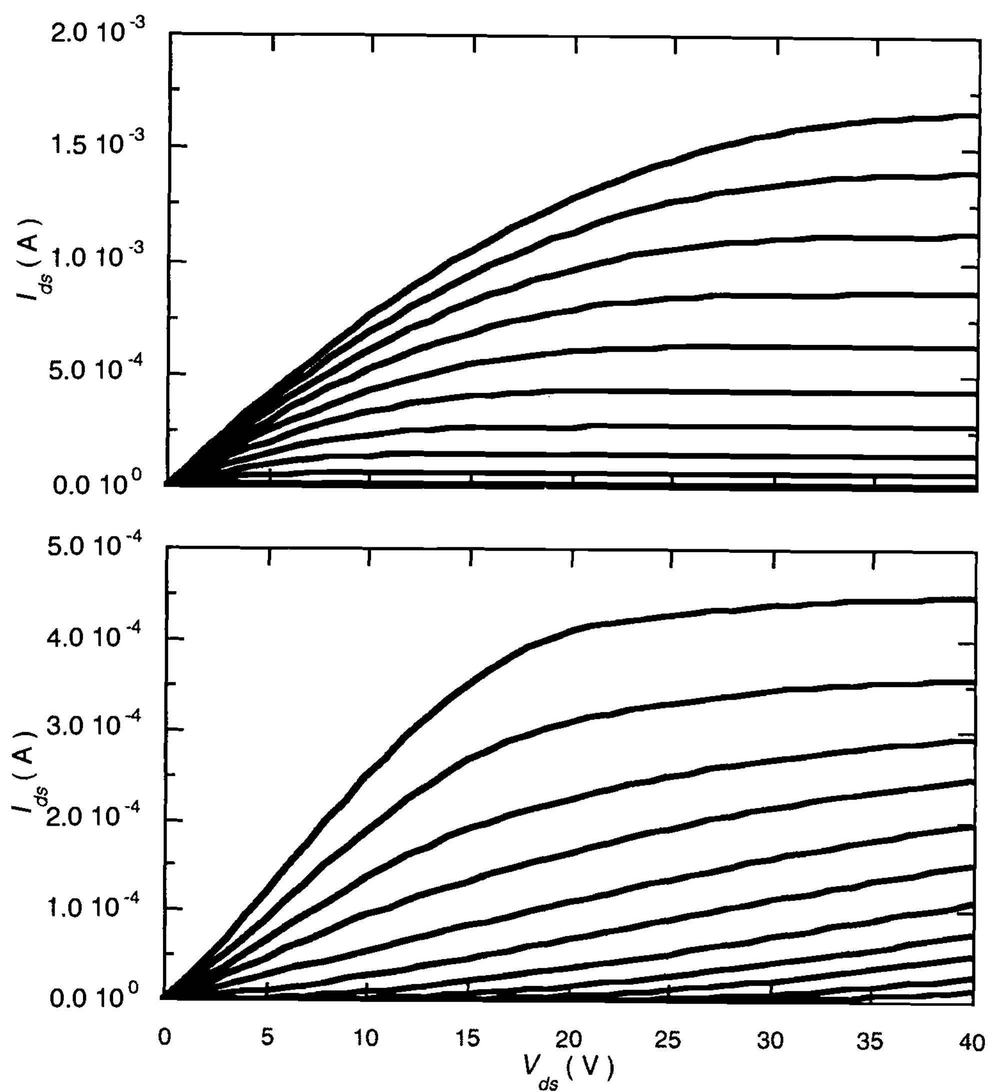

Figure 6.5: I_{ds}-V_{ds} characteristics of transistor ZTO_045A from the first analysis (top) compared to the second analysis performed three days later (bottom). Each curve corresponds to a 4 V increment in gate voltage, with the bottom curve at V_{gs} = 0 V, and the top curve at V_{gs} = 40 V.

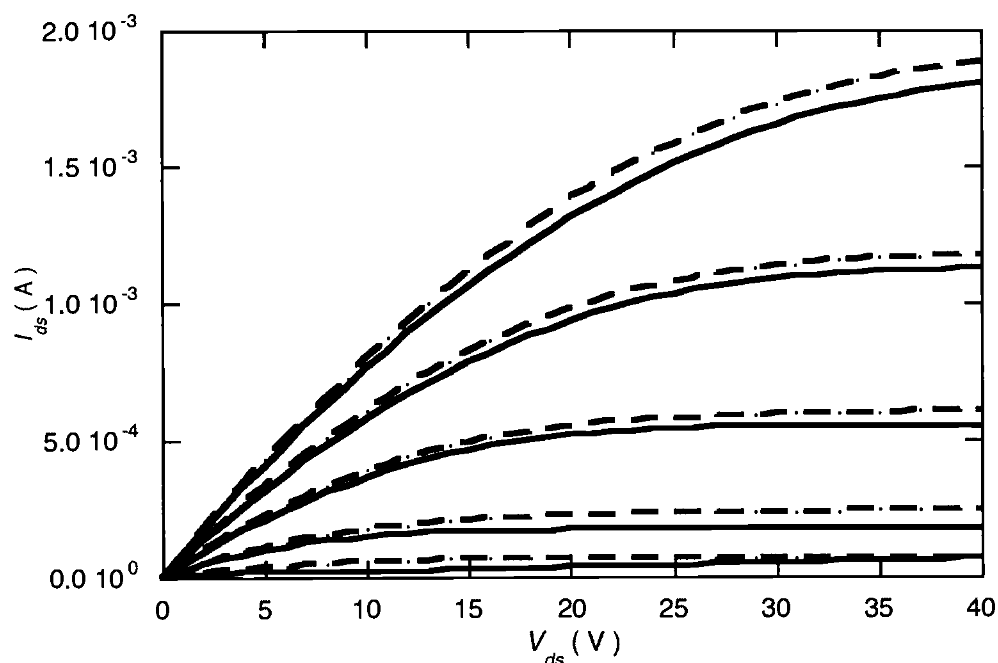

Figure 6.6: A ZTO TTFT channel layer directly after 100 °C anneal (solid), and after another week of storage (dashed). Each curve corresponds to a 10 V increment in gate voltage, with the bottom curve being at V_{gs} = 0 V and the top curve at V_{gs} = 0 V.

The degradation to soft saturation is also observed for sputtered ZTO TTFTs processed by Emma Kettenring of Oregon State University's EECS department. The 100 °C anneal is observed to improve saturation characteristics in these devices. An example of this is shown in Figure 6.7.

In Figure 6.7, it is observed, especially at low gate voltages, that the soft saturation occurs after one month. The current drive increases as well. The low temperature annealing process reverses the degradation and causes the device to exhibit hard saturation once again.

A possible explanation for this degradation is that after exposure to ambient laboratory conditions, gases are adsorbed onto the surface. These adsorbed gases modulate the channel conductivity by drawing carriers away from the induced channel. Therefore, the film behaves as a combination of a variable resistor, and a

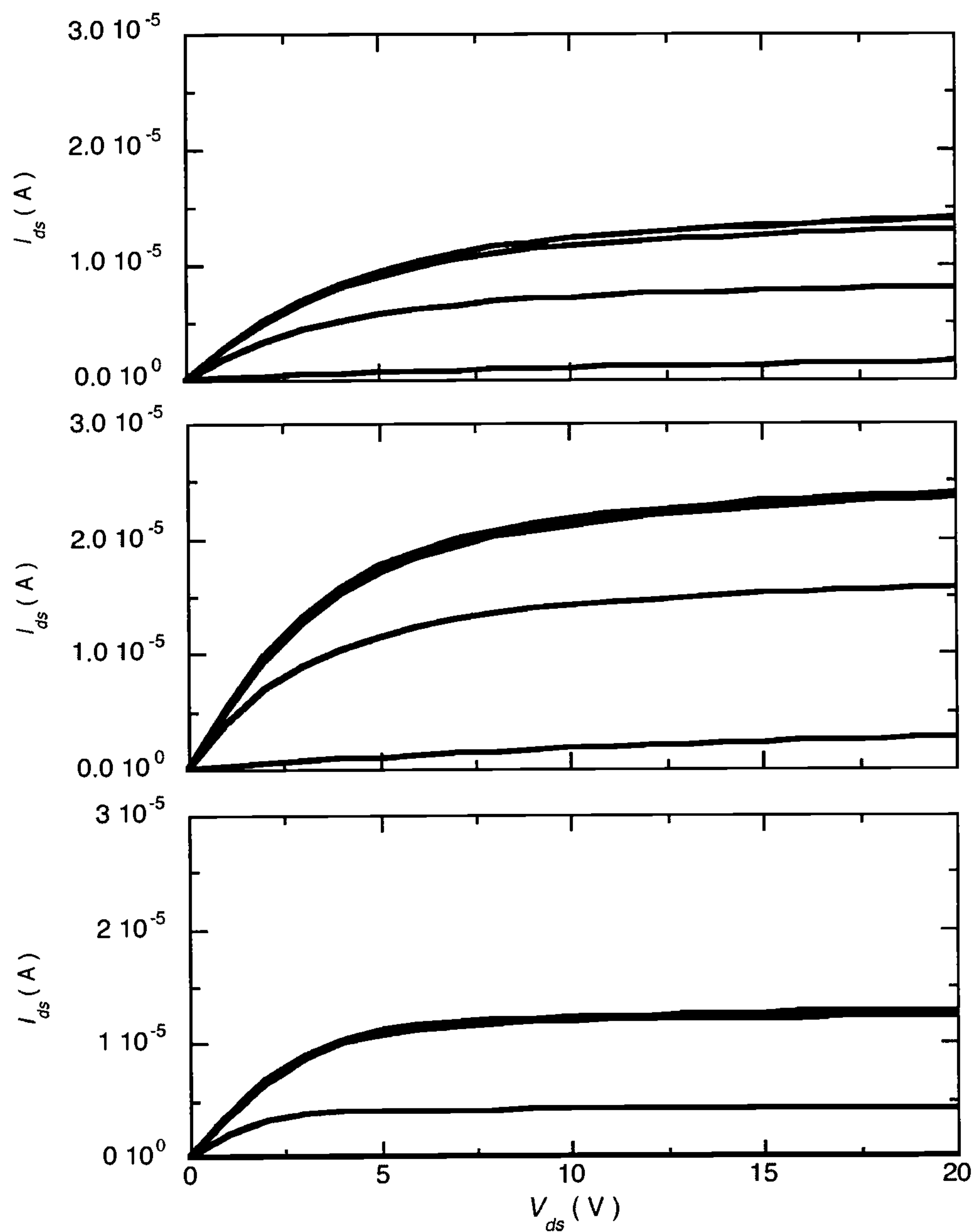

Figure 6.7: I_{ds}-V_{ds} characteristics for a sputtered ZTO TTFT after processing (top), after one month in ambient conditions (middle), and after a 100 °C anneal (bottom). Gate voltages are (from bottom to top curve in each plot) -10 V, -2 V, 2 V, 6 V, and 10 V.

transistor, as seen in the bottom I_{ds}-V_{ds} plot in Figure 6.5 and in the middle plot in Figure 6.7. The increased current drive observed in Figure 6.7 after degradation

can be attributed to a conductive surface layer being formed. Though the current drive is higher, it is not well controlled by the gate. To eliminate this surface layer by desorption, films that have shown degradation are annealed at 100 °C. This temperature is low enough not to cause a structural change of the ZTO. Films that show degradation to soft saturation are improved by the annealing process. The mobility is found to decrease after the anneal, but mobility for the degraded devices is not meaningful because the devices are not true transistors.

A film is produced under the same conditions of ZTO_045 (Appendix A), but is deposited onto a heated substrate at 600 °C in place of the post-deposition anneal. This film is too conducting to work as a transistor channel layer and behaves as a resistor. A simple two-point resistance measurement shows a resistance of a few kΩ across 1 cm of film.

Transmission in the visible and UV are measured for TTFTs ZTO_038, ZTO_039, and ZTO_040 (Appendix A) which are deposited from the 1.8:1, 2.0:1, and 2.2:1 targets, respectively. All these devices are annealed at 600 °C. The scan is taken in the center of the channel layer, between the source and drain contacts. Figure 6.8 shows the direct transmittance of the stack of ZTO, ATO, ITO, and glass substrate for these three channel layers.

Of these devices, the maximum transmittance achieved is approximately 80% for ZTO_040. Recall from the EPMA results that the films are generally ZnO deficient. Therefore, the films made from the 2.2:1 target are most likely the closest to the 2.0:1 zinc-to-tin stoichiometry.

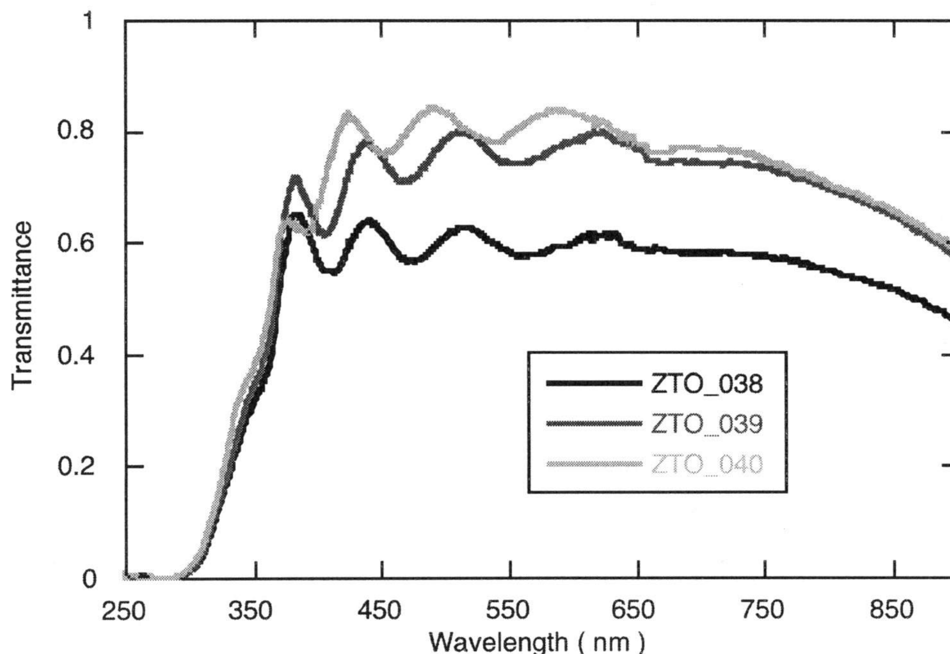

Figure 6.8: Transmittance (direct) for three transistor channel layers on ITO/ATO/glass substrates. The source and drain contacts were not included in the stack.

6.4 Summary

Out of 11 different TTFTs with no post-deposition annealing, only one shows transistor-like behavior. This result, however, is not reproducible. $I_{on:off}$ for this film is only 10 and the mobility is less than 0.0025 cm^2-V^{-1}-s^{-1}. The devices that fail either show resistor like behavior with linear I_{ds}-V_{ds} characteristics, gate voltage modulated resistance, or 'quasi-transistor' behavior with all gate voltages above 0 V resulting in the same general transistor-like I_{ds}-V_{ds} curve saturating in the low nA range. Annealed devices show improved transistor behavior, with the 300 °C anneal resulting in devices with $I_{on:off}$ in the 10^2 range, and low (0.004 cm^2-V^{-1}-s^{-1}) mobilities. The 600 °C annealed devices have $I_{on:off}$ in the 10^5 range, incremental mobilities as high as 8.35 cm^2-V^{-1}-s^{-1}, and average mobilities as high

as 6.63 cm^2-V^{-1}-s^{-1}. The mobilities obtained for TTFTs fall within the range measured by the HMS on the van der Pauw structures.

Some of the films' electrical properties degrade with time in ambient laboratory conditions. This is thought to be caused by surface absorption from the atmosphere, which induces a layer of increased conductivity on the surface. This leads to decreased gate-voltage control of the channel layer conductivity. A low temperature (100 °C) anneal improves the degraded devices by desorption of this surface layer.

Improvement in saturation is observed for all degraded devices following the low temperature annealing process. This degradation could also be avoided by adding a protective coating over the finished device as a last step in device manufacture. For future TTFT measurements, it is advised to analyze films directly after manufacture.

The most effective parameter for producing good TTFTs is a 600 °C anneal. Oxygen deposition pressure has a lesser effect on device performance, with 10^{-2} Torr being optimal. Target Zn-to-Sn ratio had a very minor effect on device performance.

In summary, TTFTs are successfully manufactured. Post-deposition annealing of the channel layer is essential for creating a functional device. This anneal results in films becoming a mixture of primarily amorphous ZTO, with the inclusion of some nanocrystalline ZnO and a possibility of crystalline SnO_2 and ZTO. Pure amorphous films do not produce functional TTFTs, nor do a films deposited at a PLD substrate temperature of 600 °C.

Chapter 7
CONCLUSIONS AND FUTURE WORK

7.1 Conclusions

For ZTO TTFT channel layers deposited by PLD, the most effective processing parameter for improved device performance is a 600 °C post-deposition anneal. The next most effective parameter is the oxygen deposition pressure, with the optimum pressure being in the 10^{-2} Torr range. Target zinc-to-tin ratio seems to have little effect on device performance within the ranges tested.

For films, the highest Hall mobility obtained is 10.4 cm^2-V^{-1}-s^{-1} with a resistivity of 1.73 Ω-cm for a film deposited in oxygen at 8.91 x 10^{-3} Torr from the 2.2:1 target. For transistor channel layers, insulating films ($\rho > 100$ MΩ–cm) are desired. The best transistor channel layers are deposited with oxygen deposition pressures in the 10^{-2} Torr range from the 2.2:1 target, though good results are also obtained from the 1.8:1 target deposited in the 10^{-3} Torr range. These films are annealed in air at 600 °C to produce transistor channel layers.

Optical analysis gives $\frac{T}{1-R}$ for these films to be greater than 90%, on average. The analysis for the optical bandgap on these films gives energies of 3.03 to 3.70 eV, which encloses the 3.35 eV direct bandgap for crystalline Zn_2SnO_4.

Compositional analysis shows the films are zinc deficient when compared to their respective target's stoichiometry. Laser energy density and oxygen pressure during deposition has a minor influence on the films' Zn-to-Sn ratio. Stoichiometric transfer of ZTO from target to film using PLD does not occur, with films generally having a Zn to Sn ratio of 15% less than that of the targets.

XRD analysis shows that films deposited onto room temperature substrates are amorphous. After a 600 °C anneal, the film analyzed remains predominately amorphous ZTO with the inclusion of some crystalline ZnO.

The transistor channel layers produced without a post-deposition anneal fail to show transistor behavior. Transistor characteristics improve after a 300 °C anneal, and more so with a 600 °C anneal. Current on-to-off ratios of 10^5 are achieved, with average and incremental mobilities as high as 6.63 cm^2-V^{-1}-s^{-1} and 8.35 cm^2-V^{-1}-s^{-1}, respectively. These transistor characteristics of PLD-deposited ZTO channel layers are slightly inferior to the RF-magnetron sputtered ZTO channel layers reported by Chiang with field-effect mobilities of 50 cm^2-V^{-1}-s^{-1} and current on-to-off ratios of 10^8 (Chiang 2003), and are improved over sputter-deposited SnO_2 layers with peak mobilities of 2.0 cm^2-V^{-1}-s^{-1} and current on-to-off ratios of 10^5 (Presley *et al.* 2004).

ZTO TTFTs show non-ideal behavior with storage in atmosphere over a time scale of a few days. This degradation is most likely caused by surface adsorption of impurities from atmosphere that modulate the channel conductance by drawing carriers from the channel. A 100 °C anneal improves these degraded devices by desorbing impurities from this surface layer. This degradation could be avoided in manufacturing by adding a protective coating to the finished device. It is suggested that for future TFT measurements, the analysis is carried out for each device directly after manufacturing.

There continues to be an interest in TTFTs fueled by a growing market for transparent electronics. Many TCOs contain elements such as cadmium or indium, which are toxic or rare. ZTO is a viable alternative and is abundant and non-toxic. ZTO is versatile, since it can be made conducting (Young 2000) for uses such as thin-film photovoltaics, electrochromic devices, low-e windows, and flat panel displays (Perkins *et al.* 2002a) or insulating enough to make enhancement-mode devices.

7.2 Future Work

This body of work leaves much to be investigated for future projects. The first step in continuing this work would be to manufacture and test more annealed devices made from the current targets with varying deposition pressures. The deposition pressures have been categorized into three types in this work: high pressure ~ 10^2 Torr range, medium pressure ~ 10^3 Torr range, and vacuum with no oxygen admitted into the system. An annealed device from the 1.8:1 target remains to be made at high deposition pressure, as well as from the 2.0:1 target at both high and vacuum pressures, and from the 2.2:1 target, at vacuum pressure. Completing this set may give more insight into which targets are ideal for device performance and how to further adjust the target zinc-to-tin ratios for improved devices.

The parameter of annealing temperature is not thoroughly investigated, and it is quite possible that temperatures above 600 °C will yield more crystalline films. The effect of crystallinity on device performance could be studied, and an optimal annealing temperature and time could be found.

XRD analyses should be carried out for more annealed films in order to fully understand the effects of the annealing process.

BIBLIOGRAPHY

Brown, R. D., http://minerals.usgs.gov/minerals/pubs/commodity/indium/index.html#myb, (2004).

Chiang, H. Q., Master's Thesis, Oregon State University, (2003).

Chiang, H. Q., Hoffman, R. L., Wager, J. F., Jeong, J., Keszler, D. A., to be published (2004).

Choi, B. H., Im, H. B., Song, J. S., Yoon, K. H., *Thin Solid Films* 193 (1990): 712-720.

Chopra, K. L., Major, S., Pandya, D. K., *Thin Solid Films* 102, 1 (1982): 1-46

Claeyssens, F., Cheesman, A., Henley, S. J., Ashfold, M. N. R., *J. Appl. Phys.* 92, no. 11 (2002): 6886-6894.

Coutts, T. J., Young, D. L., Li, X., Mulligan, W. P., Wu, X., *J. Vac. Sci. Technol. A* 18, no. 6 (2000): 2646-2660.

Dates, H. F., Davis, J. K., U.S. Patent No. 3,331,702 (1967).

Exarhos, G. J., *Characterization of Optical Materials* (Massachusetts: Butterworth Heinemann, 1993).

Gordon, R. G., *MRS Bulletin* 25, no. 8 (2000): 52-57.

Gordon, R. G., U.S. Patent No. 4,146,657 (1979).

He, T., Ehrhart, P., Meuffels, P., *J. Appl. Phys.* 79, no. 6 (2001): 3219-3223.

Hishikawa, Y., Nakamura, N., Tsuda, S., Nakano, S., Kishi, Y., Kuwano, Y., *Japanese Journal of Applied Physics* 30, no. 5 (1991): 1008-1014.

Hoffman, R. L., *J. Appl. Phys.* 95, no. 10 (2004): 5813-5819.

Hoffman, R. L., Norris, B. J., Wager, J. F., *Appl. Phys. Lett.* 82, no. 5 (2003): 733-735.

Hu, J. Gordon, R. G., *J. Appl. Phys.* 72, no. 11 (1992): 5381-5392.

Hu, J., Gordon, R. G., *Microcrystalline Semiconductors: Materials Science & Devices,* edited by Fauchet, P. M., Tsai, C. C., Canham, L. T., Shimizu, I., Aoyagi, Y., (Mater. Res. Soc. Symp. Proc. 283, Pittsburgh, 1993): 891.

Hu, J., Gordon, R. G., *J. Appl. Phys.* 71, no. 2 (1992): 880-890.

Hu, J., Gordon, R. G., *Sol. Cells,* 30 (1990): 437.

Kilcher, L., Senior Thesis, Oregon State University (2002).

Kluth, O., Agashe, C., Hüpkes, J., Müller, J., Rech, B., "Magnetron Sputtered Zinc Stannate films for Silicon Thin-film Solar Cells" (paper presented at the 3rd World Conference on Photovoltaic Energy Conversion, Osaka, Japan, 2003).

Lake Shore, *Lake Shore 7500/9500 Series User's Manual* (1999): A1-A17.

Lytle, W. O., Junge, A. E., U.S. Patent No. 2,566,346 (1951).

Major, S., Banerjee, A., Chopra, K. L., *Thin Solid Films* 122 (1984): 31-43.

Masuda, S., Kitamura, K., Okumura, Y., Miyatake, S., Tabata, H., Kawai, T., *J. Appl. Phys.* 93, no. 3 (2003): 1624-1630.

McGraw, J. M., Parilla, P. A., Schulz, D. L., Alleman, J., Wu, X., Mulligan, W. P., Ginley, D. S., Coutts, T. J., *Film Synthesis and Growth Using Energetic Beams*, edited by Atwater, H. A., Dickinson, J. T., Lowndes, D. H., Polman, A. (Mater. Res. Soc. Symp. Proc., 388, Pittsburgh, 1995): 51.

McMaster H. A., U.S. Patent No. 2,429,420 (1947).

Minami, T., *MRS Bulletin* 25, no. 8 (2000): 38-44.

Minami, T., Nanto, H., Takata, S., *Jpn. J. Appl. Phys., Part 2: Lett.* 23, no. 5 (1984): L280-L282.

Minami, T., Sato, H., Nanto, H., Takata. S,. *Jpn. J. Appl. Phys., Part 2: Lett.* 24, no. 10 (1985): L781-L784.

Mochel, J. M., U.S. Patent No. 2,564,706 (1947).

Nomura, K., Ohta, H., Ueda, K., Kamiya, T., Hirano, M., Hosono, H., *Science* 300 (2003): 1269-1272.

Norris, B. J., Anderson, J., Wager, J. F., Keszler, D. A., *J. Phys. D: Appl. Phys.* 36 (2003): L105-L107.

Nozik, A. J., Haacke, G., U.S. Patent No. 3,957,029 (1976).

Nozik, A. J., U.S. Patent No. 3,811,953 (1974).

Park, C-H., Private Communication (2004).

Perkins, J. D., del Cueto, J. A., Alleman, J. L., Warmsingh, C., Keyes, B. M., Gedvilas, L. M., Parilla, P. A., To, B., Readey D. W., Ginley, D. S., *Thin Solid Films* 411 (2002): 152-160.

Perkins, J. D., del Cueto, J. A., Alleman, J. L., Warmsingh, C., Keyes, B. M., Gedvilas, L. M., Parilla, P. A., Li, X., To, B., Readey, D. W., Van Hest, M., Ginley, D. S., *Conference Record of the IEEE Photovoltaic Specialists Conference* (2002): 1126-1129.

Pierret, R. F., *Semiconductor Device Fundamentals* (Massachusetts: Addison-Wesley, 1996).

Pouchou, J. L., Pichoir, F., *Scanning,* 12, (1999): 212-224.

Presley, R. E., Munsee, C. L., Park, C-H., Hong, D., Wager, J. F., Keszler, D., A., *J. Phys. D: Appl. Phys.* 37 (2004).

Qiu, S. N., Qiu, C. X., Shih, I., *Sol. Energy Mater.* 15 (1987): 261.

SAMx, STRATAgem Manual, Software Version 3.0, La Valirére, France (2003).

Tucker, D., Senior Thesis, Oregon State University (2002).

Urbach, F., *Phys. Rev.* 92 (1953): 1324.

van der Pauw, I. J., *Philips Research Reports.* 13, no. 1, (1958): 1-9.

Vijayakumar, P. S., Blaker, K. A., Weiting, R. D., Wong, B., Halani, A. T., Park, C., U.S. Patent No. 4,751,149 (1988).

Weimer, P. K., "The TFT – a new thin-film transistor," *Proceedings of the IRE*, vol. 50 (1962): 1462-1469.

Wu, X., Mulligan, W. P., Coutts, T. J., "Electrical and Optical Properties of Transparent Conducting Cadmium Stannate and Zinc Stannate Thin-films prepared by RF Magnetron Sputtering" (paper presented at the Society of Vacuum Coaters 39th Annual Technical Conference Proceedings, Philadelphia, PA. 1996).

Young, D., Ph.D. Thesis, Colorado School of Mines (2000).

Young, D., L., Williamson, D. L., Coutts, T., J., *J. Appl. Phys* 91, no. 3 (2002): 1464-1471.

APPENDICES

APPENDIX A

PLD Deposited Films

Film #	Target [ZnO/SnO2]	O2 Pressure	Energy Density [J/cm2]	Total Pulses [±50]	Beam Area [cm2]
8	2.0	1.04E-02	2.08	15000	0.108
9	2.0	1.04E-02	1.46	8700	0.108
10	1.8	1.06E-02	1.38	6000	0.108
11	1.8	1.06E-03	1.27	3000	0.108
12	2.2	1.00E-02	1.29	2000	0.108
13	2.0	5.00E-02	1.29	2520	0.108
14	2.0	5.04E-02	1.21	6000	0.108
16TR	2.2	1.05E-02	1.42	2850	0.108
17	2.0	5.07E-02	1.29	2520	0.108
18	2.2	1.06E-02	1.21	2100	0.108
19	2.2	7.00E-07	1.23	6000	0.108
20	2.0	2.00E-02	1.70	3000	0.13
21	2.0	8.91E-03	1.69	3000	0.13
22	2.2	6.00E-03	1.59	3000	0.13
23	2.2	7.12E-03	1.11	3000	0.13
24	2.2	4.04E-02	1.08	3600	0.13
25TR	2.2	6.98E-03	3.17	3600	0.067
26TR	2.2	3.00E-07	3.24	3600	0.067
27TR	2.2	5.94E-02	2.96	6000	0.067
28TR	1.8	3.35E-07	2.96	6000	0.067
29TR	2.0	6.01E-03	2.96	6000	0.067
30TR	1.8	6.08E-02	2.98	6000	0.067
31TR	2.0	5.93E-02	2.99	6000	0.067
32	2.2	1.00E-02	2.37	6000	0.067
33	2.0	9.96E-03	1.77	6000	0.067
34TR	2.0	7.00E-07	1.67	6000	0.108
35TR	1.8	1.20E-07	1.88	6000	0.067
36TR	1.8	6.00E-03	1.91	6000	0.067
37TR	1.8	3.00E-07	1.06	6000	0.094
38TR	1.8	9.50E-04	1.05	6000	0.094
39TR	2.0	9.73E-04	1.06	6000	0.094
40TR	2.2	1.01E-03	1.02	6000	0.094
41TR	2.2	9.93E-04	1.04	6000	0.094
42TR	2.0	9.20E-04	1.04	6000	0.094
43TR	1.8	9.60E-04	1.08	6000	0.094
44	1.8	9.60E-04	1.05	6000	0.094
45TR	2.2	1.10E-02	1.32	6000	0.094
46TR*	2.2	1.00E-02	0.96	6000	0.094

Table A: PLD deposited films. O_2 pressure is in Torr. Film 46TR* was deposited onto a substrate at 600 °C. All others were deposited at ambient temperature. The densities of the targets are 97%, 98.7%, and 94% for the 2.0:1, 2.2:1, and 1.8:1 targets, respectively.

APPENDIX B

Optical Characterization Results

Film ID #	T/(1-R) @ 500nm [%]	a at 500nm [cm^{-1}]	Direct Gap Energy [eV]	Indirect Gap Energy [eV]	Thickness [nm]
8	44.6	5000	3.03	1.8	1500
9	65.7	5700	3.27	2.5	728
10	72.8	6800	3.38	2.4	465
11	78.4	15600	3.26	2.25	150
12	92.0	5600	3.64	2.51	134
13	98.0	2830	3.55	2.74	106
14	77.6	7050	3.15	2.15	340
17	94.0	8373	3.7	3.1	70
19	94.8	9400	3.42	2.41	95
21	91.3	4050	3.59	2.75	277
22	86.0	9133	3.47	2.3	164
23	92.0	7500	3.53	2.5	120
24	99.7	300	3.51	2.74	130

Table B: Transmittance, absorption coefficient, and results from the direct and indirect bandgaps analyses for several ZTO films. The low transmittance of films 8 and 9 is due to the thickness of the films.

APPENDIX C

EPMA Results for Targets

rmalized to 1 atom of Sn.					
Target	(Location) # Data Points	Zinc	Standard Deviation	Oxygen	Standard Deviation
1.8:1	12	2.03	0.16	4.02	0.19
1.8:1	12	2.00	0.03	4.15	0.06
1.8:1	12	1.88	0.21	3.86	0.23
1.8:1	12	1.86	0.08	3.99	0.11
1.8:1	12	1.82	0.07	4.06	0.11
1.8:1	(Light Area) 5	0.04	0.01	1.90	0.07
1.8:1	(Light Area) 5	0.04	0.01	1.89	0.02
1.8:1	(Light Area) 5	0.74	0.08	2.61	0.83
1.8:1	(Light Area) 5	0.13	0.12	2.00	0.15
1.8:1	(Light Area) 5	0.34	0.15	2.26	0.17
2:1	12	2.03	0.04	3.97	0.03
2:1	12	1.98	0.01	4.09	0.04
2:1	12	1.95	0.05	3.93	0.10
2:1	12	1.92	0.01	4.03	0.04
2:1	12	1.88	0.01	4.14	0.04
2.2:1	12	2.26	0.35	4.21	0.39
2.2:1	12	2.08	0.14	4.16	0.15
2.2:1	12	2.25	0.38	4.28	0.37
2.2:1	12	2.16	0.14	4.28	0.12
2.2:1	12	2.17	0.16	4.44	0.15

Table C: Summary of EPMA results for three ZTO targets. Locations of data points are random unless indicated otherwise.

APPENDIX D

TTFT Characteristics

Target Zn:Sn	O_2 Pressure [Torr]	μ_{avg} (max)	μ_{inc} (max)	I_{ds} drive at $V_{gs} = 40$ V	Anneal [°C]	$I_{On:Off}$	Film ID
1.8	3.00E-07	4.110	5.300	9.00E-04	600	1E+05	37
1.8	9.50E-04	5.890	7.290	1.20E-03	600	1E+05	38
1.8	9.60E-04	6.140	8.000	1.50E-03	600	1E+05	43
2	9.73E-04	1.270	1.590	2.00E-04	600	1E+05	39
2.2	1.01E-03	1.040	1.390	2.75E-04	600	1E+05	40
2.2	1.10E-02	6.630	8.350	1.60E-03	600	1E+05	45A
2.2	1.10E-02	1.730	4.620	4.00E-04	600	1E+05	45A-2nd run
2	9.20E-04	0.004	0.004	2.25E-07	300	1E+02	42
2.2	9.93E-04	0.005	0.006	3.50E-07	300	2E+02	41
1.8	1.20E-07	X	X	X	None	X	35
1.8	6.00E-07	X	X	6.00E-08	None	10	28
1.8	6.00E-03	X	X	X	None	X	36
1.8	6.08E-02	X	X	X	None	X	30
2	7.00E-07	X	X	X	None	X	34
2	6.01E-03	X	X	X	None	X	29
2	5.93E-02	X	X	X	None	X	31
2.2	3.00E-07	X	X	X	None	X	26
2.2	6.98E-03	X	X	X	None	X	25
2.2	1.10E-02	X	X	X	None	X	45B
2.2	5.94E-02	X	X	X	None	X	27

Table D: μ_{avg}, μ_{inc}, saturation current at 40 V gate voltage, and $I_{on:off}$ for the TTFT channel layers tested. "X" indicates a device that doesn't work.